

Collective excitations in the critical regime of superfluid Fermi gases

S. N. Klimin

TQC, Universiteit Antwerpen, Universiteitsplein 1, B-2610 Antwerpen, Belgium

J. Tempere

*TQC, Universiteit Antwerpen, Universiteitsplein 1, B-2610 Antwerpen, Belgium and
Lyman Laboratory of Physics, Harvard University, USA*

H. Kurkjian

TQC, Universiteit Antwerpen, Universiteitsplein 1, B-2610 Antwerpen, Belgium

(Dated: December 23, 2024)

Abstract

Studying the collective pairing phenomena in a two-component Fermi gas, we predict the appearance near the transition temperature T_c of a well-resolved collective mode of quadratic dispersion. The mode is visible both above and below T_c in the system's response to a driving pairing field. When approaching T_c from below, the phononic and pair-breaking branches, characteristic of the zero temperature behavior, reduce to a very low energy-momentum region when the pair correlation length reaches its critical divergent behavior $\xi_{\text{pair}} \propto |T_c - T|^{-1/2}$; elsewhere, they are replaced by the quadratically-dispersed pairing resonance, which thus acts as a precursor of the phase transition. In the strong-coupling and Bose-Einstein Condensate regime, this mode is a weakly-damped propagating mode associated to a Lorentzian resonance. Conversely, in the BCS limit it is a relaxation mode of pure imaginary eigenenergy. At large momenta, the resonance disappears when it is reabsorbed by the lower-edge of the pairing continuum. At intermediate temperatures between 0 and T_c , we unify the newly found collective phenomena near T_c with the phononic and pair-breaking branches predicted from previous studies, and we exhaustively classify the roots of the analytically continued dispersion equation, and show that they provided a very good summary of the pair spectral functions.

I. INTRODUCTION

The present theoretical investigation is devoted to oscillation-like and relaxation-like collective excitations of atomic Fermi superfluids (see, for review, Ref. [1, 2]) in the crossover between the Bardeen-Cooper-Schrieffer (BCS) pairing regime and the opposite limit of the Bose-Einstein condensation (BEC) of molecules. An increasing interest to collective excitations in condensed Fermi gases has been recently inspired by experimental achievements [3–9]. Particularly, in Refs. [8, 9], the spectral function of the density response of a Fermi gas has been experimentally investigated at finite momentum and temperature.

The state-of the art of the theory of collective excitations in atomic Fermi gases shows that there are still unexplored areas, in particular away from the low-temperature, low-momentum regime. Combescot *et al.* [10] and Diener *et al.* [11] analyzed the dispersion of phononic (Anderson-Bogoliubov) collective excitations in a wide range of momentum at zero temperature. An analytic study of the dispersion of phonons has been performed in Ref. [13], still at $T = 0$. Ohashi and Griffin [12] studied the order-parameter response functions at $T \neq 0$ and identified a resonance interpreted as a damped phononic collective mode. Last, the nonzero-temperature phonon lifetime has been calculated using the perturbation scheme [14] at low temperature, and beyond the perturbative regime using the analytic continuation of the Gaussian pair fluctuation (GPF) propagator [15] at higher temperature, in particular near T_c .

Besides phononic modes, superconductors and Fermi superfluids also support a pair-breaking (sometimes called “Higgs”) collective branch. This branch, which is intrinsically related to the existence of a pair-breaking continuum [16, 22] in the quasiparticle spectrum, has been analytically investigated for atomic Fermi gases in the BCS–BEC crossover at zero temperature [17]. At $T \neq 0$, Ref. [18] predicted that a pair-breaking mode very similar to the zero-temperature one exists as long as the wavelength is much larger than the size of the Cooper pairs.

Near the transition temperature T_c , the gas enters a critical regime where the pair correlation length diverges (according to BCS approximation) as $\xi_{\text{pair}} \propto |T_c - T|^{-1/2}$ and the order parameter Δ vanishes (below T_c) as $(T_c - T)^{1/2}$. The size of this critical regime should be comparable to T_c at unitarity [27] but decrease as $(T_c/\epsilon_F)^4$ in the BCS limit and as $k_F a_s$ in the BEC limit (where a_s is the s -wave scattering length and ϵ_F , k_F respectively

the Fermi energy and wavevector). In this critical regime, the region where phononic and pair-breaking modes exist reduces to energies $\lesssim \Delta$ and momenta $\lesssim 1/\xi_{\text{pair}}$. The question of whether collective excitations characteristic of the onset of a superfluid phase are still visible in the critical regime, at wavevectors low or comparable to the Fermi wavevector k_F is thus still open.

Here, we show that the dispersion equation supports a collective branch of quadratic start at and near T_c . This mode is a weakly-damped propagating mode at strong coupling (it is even undamped in the BEC regime) and a relaxation mode (of a purely imaginary frequency) in the BCS limit. It generates a well-resolved resonance in the pair spectral function in the whole BEC-BCS crossover. Observable also at $T > T_c$ provided one can drive the formation of pairs in the system (for example by coupling it to a reservoir of superfluid pairs) this mode acts as a precursor of the superfluid phase transition. Above T_c , it signals that Cooper pairs injected into the system subsist longer as the temperature approaches T_c , just like ice subsists longer in liquid water whose temperature approaches 0°C . After its quadratic depart, the resonance disappears at wavevectors $q \gtrsim k_F$ when it is absorbed by the rising lower edge of the pairing continuum.

At intermediate temperatures between 0 and T_c , we supplement existing studies by performing an exhaustive cartography of the roots of the dispersion equation at all momenta, exploring all possible windows of analytic continuation. The eigenfrequencies and damping factors are determined here mutually consistently, i. e., beyond the perturbative approximation for damping. A key advantage of our exhaustive study is that all collective excitation branches are brought together within a unified approach. In particular, we explain that the newly found collective pairing mode at $T = T_c$ differs in nature from the phononic and pair-breaking branches: its emergence when $T \rightarrow T_c$ is caused by distinct poles of the analytic continuation. Finally, we compare the spectral function to its estimate based on the poles (and associated residues) found in the analytic continuation, finding a very good agreement between the two.

II. METHOD

We consider here a superfluid Fermi gas with s -wave pairing. Both equilibrium and response properties can be determined from the partition function of the fermionic system.

Within the path integral formalism [11, 16, 20], the partition function is a path integral over Grassmann variables $(\bar{\psi}_\sigma, \psi_\sigma)$, which replace the second quantization operators. The model fermionic action is given by:

$$S = \int_0^\beta d\tau \int d\mathbf{r} \left[\sum_{\sigma=\uparrow,\downarrow} \bar{\psi}_\sigma \left(\frac{\partial}{\partial \tau} - \frac{\nabla_{\mathbf{r}}^2}{2m} - \mu \right) \psi_\sigma + g \bar{\psi}_\uparrow \bar{\psi}_\downarrow \psi_\downarrow \psi_\uparrow \right], \quad (1)$$

where we have set $\hbar = k_B = 1$. Here $\beta = 1/T$ is the inverse to temperature, μ is the chemical potential, and $g < 0$ is the bare coupling strength of the model s -wave contact interaction. This coupling constant is renormalized at fixed the scattering length a_s by the relation: [20]:

$$\frac{1}{g} = \frac{m}{4\pi a_s} - \int_{k < k_c} \frac{d^3k}{(2\pi)^3} \frac{m}{k^2} \quad (2)$$

where k_c is the cutoff momentum. Further on, we apply the limit $k_c \rightarrow \infty$, which leads to the contact interaction constant $g \rightarrow 0$.

The Hubbard-Stratonovich transformation introducing the bosonic pair field $[\bar{\Psi}, \Psi]$ with the subsequent integration over the fermion fields results in an effective bosonic action [11, 15]. Within the Gaussian pair fluctuation (GPF) approximation, collective modes for a superfluid Fermi gas appear as fluctuations of this bosonic action on top of the uniform background saddle-point value Δ of the pair field. In the present work, background values of the gap Δ and the chemical potential μ are calculated within the mean-field approximation. This gives us a qualitatively adequate description of the collective excitations. For a better quantitative description, an equation of state beyond the mean-field approximation should be applied but this is beyond the scope of the present treatment.

We determine the spectra of collective excitations within GPF using the method of the analytic continuation of the GPF matrix elements through their branch cuts, as proposed by Nozières [21]. Because the formalism remains the same as in our preceding works on collective excitations [15, 17], the scheme of the calculation is reproduced here only briefly. The complex eigenfrequencies of collective excitations are determined as the roots of the determinant of the inverse GPF propagator,

$$\det \mathbb{M}_\downarrow(\mathbf{q}, z_{\mathbf{q}}) = 0 \quad (3)$$

The matrix elements of \mathbb{M} , derived in Refs. [14–16] (see *e.g.* Eqs. (10) and (11) in [15]), have a branch cut all along the real axis, such that roots of (3) are found only in the matrix \mathbb{M}_\downarrow analytically continued to the lower-half complex plane.

Whereas \mathbb{M} describes the fluctuations of the order-parameter in the cartesian basis $(\delta\Delta, \delta\Delta^*)$, it is often easier to deal with fluctuations in the phase-modulus (or phase-amplitude by a misuse of language we allow ourselves here) basis $(\delta(\arg\Delta), \delta|\Delta|)$ (this is particularly the case at low-temperature and momentum where phase and modulus fluctuations are well decoupled). The fluctuation matrix in this basis is

$$\mathbb{Q} = P^\dagger \mathbb{M} P \quad (4)$$

where P is the hermitian matrix $\begin{pmatrix} 1 & i \\ 1 & -i \end{pmatrix} / \sqrt{2}$. The matrix elements of \mathbb{Q} ($Q_{1,1}$ and $Q_{2,2}$ correspond to the amplitude and phase fluctuations, respectively, and $Q_{1,2}$ describe mixing of amplitude and phase fluctuations) are given in appendix A.

Strictly speaking, complex poles of Green's functions in a condensed matter theory can be reliably interpreted as eigenfrequencies and damping factors of collective excitations or quasiparticles when the damping factors are relatively small with respect to eigenfrequencies. Nevertheless, they have a heuristic value even when damping is not small, as long as they bring significant contributions to the pair field and density spectral functions. Complex poles of the GPF propagator can reveal the analytic structure and the physical origin of the shape of the spectral functions, even when this shape is not a simple Lorentzian peak. In fact, we will show in Sec. IV D that the poles found in the analytic continuation (together with their associated residues) often constitute an excellent summary of the spectral function, even when their imaginary part is comparatively large. This makes the present study relevant for an explanation of experiments on response properties of cold gases.

III. COLLECTIVE MODE NEAR THE TRANSITION TEMPERATURE

In this section, we concentrate on the collective phenomena at temperatures close to T_c . In Ref. [22], it was found that a collective mode whose eigenenergy is purely imaginary and behaves quadratically in q at low momenta ($q \ll k_F$ with $k_F = (3\pi^2 n)^{1/3}$ the Fermi wavevector in terms of the total density n) exists at and near T_c in the BCS limit ($1/k_F a_s \rightarrow -\infty$). Such collective phenomenon where an initial perturbation damps out without propagating is sometimes called a relaxation mode. On the other side of the crossover, in the BEC regime ($\mu < 0$) at $T = T_c$, Ref. [16] predicted a propagating collective mode, with a purely real eigenenergy but still a quadratic dispersion. Here, we perform a complete study of this

collective mode: we show how it evolves from a purely imaginary to a purely real mode in the BCS-BEC crossover, how its eigenenergy varies beyond the long-wavelength regime and how it is affected by small temperature deviations $|T - T_c| \ll T_c$, both below and above T_c .

A. Effective mass at $T = T_c$

Exactly at T_c , the order-parameter vanishes ($\Delta = 0$) and the fluctuation matrix becomes diagonal such that the eigenenergy of the collective mode solves simply

$$M_{11}(\mathbf{q}, z_{\mathbf{q}}) \stackrel{T=T_c}{=} \sum_{\mathbf{k}} \frac{X(\beta_c \xi_{\mathbf{q}/2+\mathbf{k}}) + X(\beta_c \xi_{\mathbf{q}/2-\mathbf{k}})}{2(z_{\mathbf{q}} - \xi_{\mathbf{q}/2+\mathbf{k}} - \xi_{\mathbf{q}/2-\mathbf{k}})} + \frac{X(\beta_c \xi_{\mathbf{k}})}{2\xi_{\mathbf{k}}} = 0 \quad (5)$$

with the inverse temperature $\beta_c = 1/T_c$, $\xi_{\mathbf{k}} = \frac{k^2}{2m} - \mu$ the free-fermion energy counted from the chemical potential μ , and the function $X(\beta\xi) = \tanh(\beta\xi/2)$. At T_c , the interaction regime can be measured by μ_c/T_c (with $\mu_c \equiv \mu(T_c)$) as an alternative to $1/k_F a_s$. The BCS and BEC limit then correspond to $\mu_c/T_c \rightarrow +\infty$ and $\mu_c/T_c \rightarrow -\infty$ respectively. In the long wavelength limit ($q \ll k_F$), the only solution of this equation varies as q^2 and is thus characterized by an effective mass m^* :

$$z_{\mathbf{q}} = \frac{\hbar^2 q^2}{4m^*} \quad (6)$$

This effective mass, shown on Fig. 1 in the BEC-BCS crossover, is found by expanding M_{11} at low q and low $z \propto q^2$:

$$\frac{m}{m^*} = \frac{C}{2D} \quad (7)$$

with

$$C = \int \frac{d\mathbf{k}}{(2\pi)^3} \frac{X(\beta_c \xi_{\mathbf{k}}) - \beta_c \xi_{\mathbf{k}} X'(\beta_c \xi_{\mathbf{k}}) - \frac{2}{3} \beta_c^2 \frac{k^2}{2m} \xi_{\mathbf{k}} X''(\beta_c \xi_{\mathbf{k}})}{8\xi_{\mathbf{k}}^2}, \quad (8)$$

$$D = D' + iD'' \quad \text{with} \quad D' = \mathcal{P} \int \frac{d\mathbf{k}}{(2\pi)^3} \frac{X(\beta_c \xi_{\mathbf{k}})}{4\xi_{\mathbf{k}}^2}, \quad \text{and} \quad D'' = \frac{\Theta(\mu)}{32\pi} \frac{(2m\mu)^{3/2}}{\mu T_c} \quad (9)$$

In the BEC regime ($\mu_c < 0$), the effective mass is real because the fermionic continuum $\xi_{\mathbf{q}/2-\mathbf{k}} + \xi_{\mathbf{q}/2+\mathbf{k}}$ is gapped (it is bounded from below by its value $2|\mu| + \frac{q^2}{4m}$ in $k = 0$) and does not damp the collective mode [20]. When going to the BEC limit ($1/k_F a_s \rightarrow +\infty$ or $\mu_c/T_c \rightarrow -\infty$), m^* tends to the fermion mass m : the collective mode there is nothing else than the dispersion relation of free bosonic dimers of mass $2m$. Higher order bosonic effects not captured by our GPF approach (such as Landau-Beliaev couplings between collective

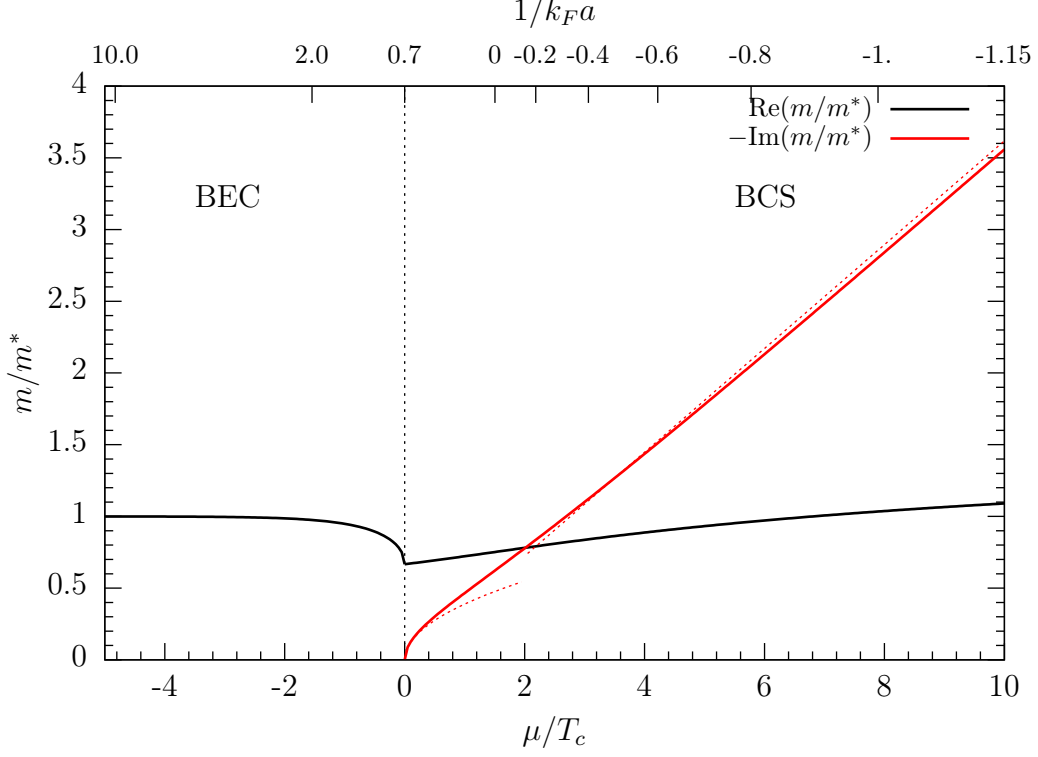


FIG. 1: The complex effective mass of the collective mode at $T = T_c$ in the BEC-BCS crossover (values of μ/T_c on the lower x -axis and $1/k_F a$ and the upper one). The red dashed lines show the limiting behavior of $\text{Im } m/m^*$ in $\mu_c/T_c \rightarrow 0^+$ and $\mu_c/T_c \rightarrow +\infty$ (see the main text).

modes) may provide additional damping channels for the collective mode, as this is the case in an atomic BECs.

In the BCS regime ($\mu_c > 0$), the fermionic continuum does reach 0, the solution $z_{\mathbf{q}}$ is found in the analytic continuation¹ of M_{11} and the effective mass acquires an imaginary part. We note the remarkable value at the threshold of the BEC regime $m/m^* = 2/3$ when $\mu_c = 0$ and the squareroot growth of the damping coefficient $\text{Im } m/m^* \underset{\mu_c \rightarrow 0^+}{\sim} -0.38\sqrt{\mu_c/T_c}$. At unitary ($1/|a_s| = 0$), the real and imaginary part are comparable: $m/m^* = 0.752 - 0.622i$. Finally, in the BCS limit ($1/k_F a_s \rightarrow -\infty$ or $\mu_c/T_c \rightarrow +\infty$), the imaginary part diverges as $\mu_c/T_c \approx \epsilon_F/T_c$

$$\frac{m}{m^*} \underset{1/k_F a \rightarrow -\infty}{\sim} -i \frac{28\zeta(3)\epsilon_F}{3\pi^3 T_c} \quad (10)$$

as found in Ref. [22]. The imaginary part thus largely dominates over the real part which

¹ The analytic continuation is here trivial: if V is the volume of the gas, one has $M_{11}(\mathbf{q}, \omega \pm i0^+)/V = C \frac{q^2}{2m} - (D' \pm iD'')\omega$ and thus $M_{11,\downarrow}(\mathbf{q}, z)/V = C \frac{q^2}{2m} - (D' + iD'')z$.

diverges only logarithmically.

B. Long wavelength behavior in the vicinity of T_c

a. Above T_c Remarkably, the collective mode found here at T_c , still persists in the normal phase $T > T_c$ as a precursor of the phase transition:

$$z_{\mathbf{q}} = \frac{q^2}{4m^*} - \alpha(T - T_c) \quad (11)$$

This equation is valid for $q^2/2m \approx |T - T_c| \ll k_F^2/2m, T_c$. It introduces the additional coefficient

$$\alpha = \frac{E}{T_c^2 D} \quad \text{with} \quad E = - \int \frac{d\mathbf{k}}{(2\pi)^3} \frac{X'(\beta_c \xi_{\mathbf{k}})}{2}. \quad (12)$$

In the BCS limit the shift $-\alpha(T - T_c)$ of the eigenenergy from its $T = T_c$ value is purely imaginary and leads to the expression $z_{\mathbf{q}} = -i \frac{28\zeta(3)}{3\pi^3} \frac{\epsilon_F}{k_B T_c} \frac{q^2}{2m} - i \frac{8(T - T_c)}{\pi}$ obtained in [22]. Physically, this means that Cooper pairs injected in the system have a shorter lifetime when the temperature rises above T_c . Correspondingly, the visibility of the collective mode fades away as one moves away from the phase transition. Conversely, in the BEC regime, the shift $-\alpha(T - T_c)$ is real positive and acts as a gap of the collective mode. In both BEC and BCS case, this shift ensures that $M_{11}(q = 0, \omega = 0)$ does not vanish in the normal phase, in accordance with the condition of Nozières – Schmitt-Rink [23] and Goldstone theorem.

Although exciting the pair spectral function above T_c is not possible using usual density-coupled probes, this can be achieved experimentally by coupling through a tunneling barrier [15] the sampled gas prepared at $T \gtrsim T_c$ to a reservoir of Cooper pairs at $T \ll T_c$, as was done for superconductors by Carlson-Goldman [24] (we note in passing the formal analogy between Eq. (11) and Eq. (18–20) in [24], although the spectrum of the mode of Carlson-Goldman is calculated in a charged fermion gas and with impurities limiting the quasiparticle lifetime).

b. Below T_c The detailed evolution of collective modes from $T = 0$ to T_c is the subject of an in-depth numerical study in the next section, but expression (6) of the collective mode can already be extended to temperatures slightly below T_c . The picture here is complexified by the presence of a small number of condensed pairs. Near T_c (and as long as μ is positive) the typical size of those pairs $\xi_{\text{pair}} = \sqrt{\mu/m\Delta^2}$ diverges, eventually becoming much larger than $1/k_F$. This opens a regime $q \lesssim 1/\xi_{\text{pair}}$ where the physics of collective

modes is similar to what exists at zero temperature (with phononic modes below 2Δ [15] and pair-breaking “Higgs” modes above [18]).

We focus here on the intermediate regime $1/\xi_{\text{pair}} \ll q \ll k_F$. Let us first remark that ignoring the presence of a gap Δ and solving the equation $M_{11}(\mathbf{q}, z_{\mathbf{q}}) = 0$ (which applies in the normal phase) leads to an unstable solution $z_{\mathbf{q}}$, with a positive imaginary part $\text{Im } z_{\mathbf{0}} \propto \beta - \beta_c$. This proves the instability of the normal phase below T_c . Instead, taking into account the deviation $M_{11}(\mathbf{q}, z, \Delta) - M_{11}(\mathbf{q}, z, 0)$ as well as the non-vanishing off-diagonal element M_{12} , one obtains the quadratic equation:

$$\left(C \frac{q^2}{2m} - iD'' z_{\mathbf{q}} - (\beta - \beta_c) E \right)^2 - (\beta - \beta_c)^2 E^2 - (D')^2 z_{\mathbf{q}}^2 = 0. \quad (13)$$

Details on the derivation of this equation are given in Appendix B. Away from the BCS limit, the two solutions of this equation are not physically distinct $z_{\mathbf{q},2} = -z_{\mathbf{q},1}^*$ with

$$z_{\mathbf{q},1} = -i \frac{CD''}{|D|^2} \frac{q^2}{2m} - i \frac{|E|D''}{|D|^2} (\beta - \beta_c) + D' \sqrt{C^2 \left(\frac{q^2}{2m} \right)^2 + 2C|E|(\beta - \beta_c) \frac{q^2}{2m}} \quad (14)$$

Here, we have neglected in the discriminant of Eq. (13) terms of order $(\beta - \beta_c)^2$. It is worth noting that although this equation is valid only for $1/2m\xi_{\text{pair}}^2 \approx \Delta^2/\mu \ll q^2/2m$ (that is for $(\beta - \beta_c)/\beta_c^2 \ll q^2/2m$), it predicts a transition from a phononic low-velocity regime $z_{\mathbf{q},1} \propto (\beta - \beta_c)^{1/2} q$ to a quadratic regime $z_{\mathbf{q},1} \propto q^2$ when extrapolated outside its validity regime to $(\beta - \beta_c)q^2/2m \approx 1$. However, we will show in section IV that in the general case (and unlike what was found in Ref. [22] for the BCS limit) the phononic branch appearing in the regime $q \approx 1/\xi_{\text{pair}}$ is supported by a distinct collective branch as the one supporting the quadratic branch $z_{\mathbf{q}}$.

In the BCS limit, the coefficient D' vanishes, and we must reincorporate the term $\propto (\beta - \beta_c)^2$ to the discriminant. We then obtain the two physically distinct solutions of Ref. [22]:

$$z_{\mathbf{q},1} = -i \frac{28\zeta(3)}{3\pi^3} \frac{\epsilon_F}{k_B T_c} \frac{q^2}{2m} \quad (15)$$

$$z_{\mathbf{q},2} = z_{\mathbf{q},1} - i \frac{16(T_c - T)}{\pi} \quad (16)$$

We note that below T_c , irrespective of the interaction regime, there exists a solution $z_{\mathbf{q}}$ which tends to 0 with q , in accordance again with the criterion of Nozières Schmitt-Rink [23].

C. Pair spectral function at arbitrary momentum

a. Pair-response and spectral functions To conclude on the observability of the collective mode, we study its manifestations in pair-field response matrix $1/M(\mathbf{q}, z)$. This response matrix quantifies the susceptibility of the system to an external complex pairing field $\varphi(\mathbf{r}, t)^* \hat{\psi}_\downarrow(\mathbf{r}) \hat{\psi}_\uparrow(\mathbf{r})$, i.e. its facility to form pairs. Generally, we expect the collective modes to manifest themselves as peaks in the spectral functions. Since the off-diagonal elements of $1/M$ (in the Cartesian basis) vanish in the limit $T \rightarrow T_c^-$ (see Appendix A), we focus here on the diagonal element:

$$\chi(\mathbf{q}, \omega) = \frac{1}{\pi} \text{Im} \frac{M_{2,2}(\mathbf{q}, \omega + i0^+)}{\det \mathbb{M}(\mathbf{q}, \omega + i0^+)} \stackrel{T=T_c}{=} \frac{1}{\pi} \text{Im} \frac{1}{M_{11}(\mathbf{q}, \omega + i0^+)}. \quad (17)$$

We also focus on the imaginary part of the response function (the spectral weight), which quantifies the capacity of the system to absorb energy injected at frequency ω .

At $T = T_c$, the matrix element $M_{1,1}$ can be expressed as the momentum integral:

$$\begin{aligned} M_{1,1}(\mathbf{q}, \omega + i0^+) \\ = \frac{1}{2\pi^2} \int_0^\infty k^2 dk \left\{ \frac{X(\beta_c \xi_{\mathbf{k}})}{2\xi_{\mathbf{k}}} + \frac{2m}{\beta k q} \ln \left(\frac{\cosh \left(\frac{\beta_c}{2} \left(\frac{(k+\frac{q}{2})^2}{2m} - \mu \right) \right)}{\cosh \left(\frac{\beta_c}{2} \left(\frac{(k-\frac{q}{2})^2}{2m} - \mu \right) \right)} \right) \frac{1}{\omega + i0^+ - 2\xi_{\mathbf{k}} - \frac{q^2}{4m}} \right\} \end{aligned} \quad (18)$$

Note that the expression above is no longer limited to long wavelengths but applies also to $q \approx \sqrt{2m|\mu|}$. The denominator of the integrand vanishes (such that $\chi(\omega)$ is nonzero) as soon as ω is above the continuum threshold $\omega_0(q) = q^2/4m - 2\mu$. In this interval, the spectral function can be expressed analytically and thus easily extended to $\text{Im } z < 0$. The analytic continuation of M_{11} through the interval $[\omega(q), +\infty[$ of the real axis is then:

$$M_{1,1,\downarrow}(\mathbf{q}, z) = M_{1,1}(\mathbf{q}, z) - \Theta(-\text{Im } z) \frac{2im}{4\pi\beta q} \ln \left(\frac{\cosh \left(\frac{1}{4}\beta_c \left(z + \frac{q\sqrt{4\mu-q^2+2z}}{2m} \right) \right)}{\cosh \left(\frac{1}{4}\beta_c \left(z - \frac{q\sqrt{4\mu-q^2+2z}}{2m} \right) \right)} \right). \quad (19)$$

where Θ is the Heaviside step function. This last expression allows us to find numerically the complex roots $z_{\mathbf{q}} = \omega_{\mathbf{q}} - i\gamma_{\mathbf{q}}$ of (5) beyond the long-wavelength quadratic regime.

b. Strong-coupling regime On Fig. 2, we show χ in function of q and ω as a color plot, together with the eigenenergy $\omega_{\mathbf{q}}$ (in green) and damping rate $\gamma_{\mathbf{q}}$ (below in red) found in the

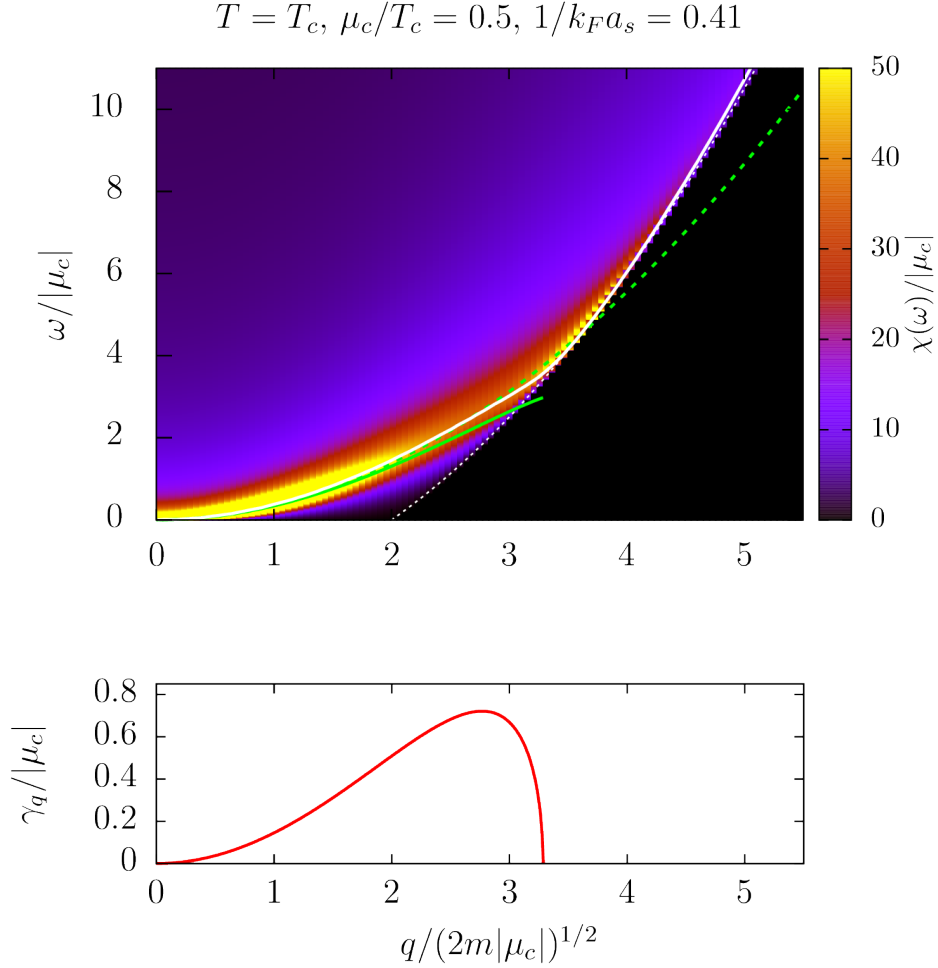


FIG. 2: (Upper pannel) The pair spectral function $\chi(q, \omega + i0^+)$ is plotted in colors as a function of q and ω at $T = T_c$ in the strong-coupling regime ($1/k_F a \simeq 0.41$ and $\mu/T_c = 0.5$, still on the BCS side of the crossover). Here and in all other figures, χ is in units of $|\mu|/\sqrt{2m|\mu|}^3$. Superimposed to the color plot are the continuum lower edge $\omega_0(q)$ (white dotted line), the collective mode eigenfrequency $\omega_{\mathbf{q}}$ (green solid), its quadratic low- q expansion (green dashed), and the numerically extracted maximum of the spectral function (white solid). (Lower pannel) The damping rate $\gamma_{\mathbf{q}}$ of the collective mode plotted in function of q with same x axis as on the upper pannel.

analytic continuation. Notice that at low q the quadratic variation of the maximum of the spectral function (white curve) is very well predicted by $\omega_{\mathbf{q}}$. As q increases the peak initially broadens and shifts to higher energy (see the blue curve in Fig. 3). At some point ($q \simeq 3$ on Fig. 2) $\omega_{\mathbf{q}}$ encounters the rising lower-edge of the continuum $\omega_0(q)$ after which the damping rate falls sharply to 0. In the spectral function this is associated with the appearance of

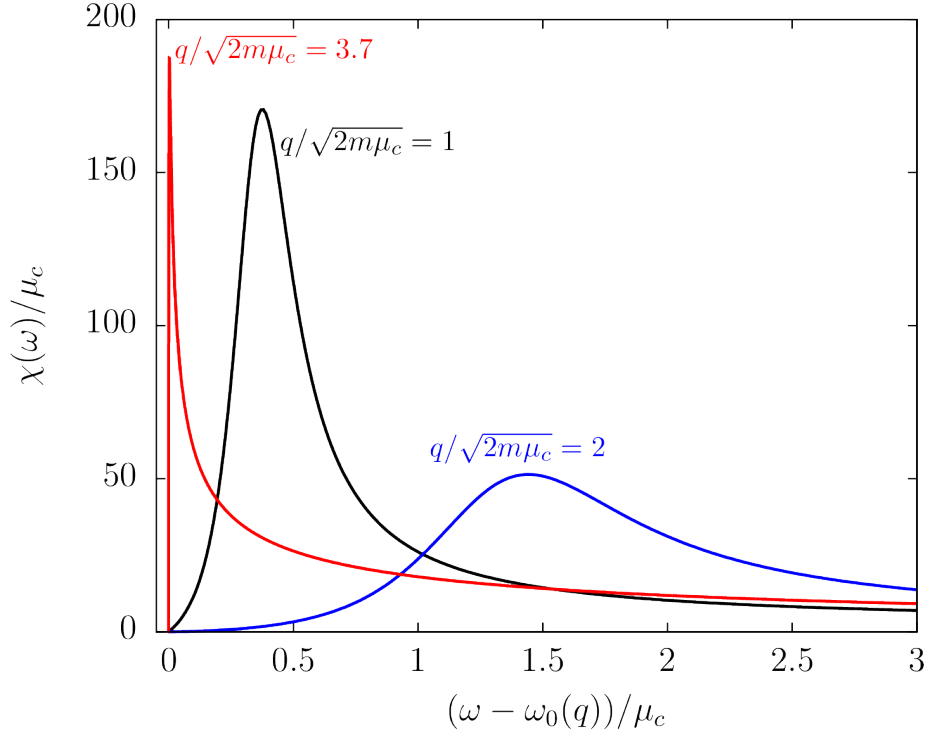


FIG. 3: At $T = T_c$ and $1/k_F a \simeq 0.41$ (same as on Fig. 2), the pair spectral function $\chi(q, \omega + i0^+)$ is plotted in function of the distance to the continuum edge $\omega - \omega_0(q)$ (with the convention $\omega_0(q) = 0$ for $q^2 < 4m\mu$) at fixed $q = 1, 2$ and 3.7 (respectively black, blue and red curves).

a very intense peak pinned at the lower edge of the continuum. However, unlike at low q , this peak of χ has a large skewness, with a sharp lower edge and a broad upper tail (red curve on Fig. 3). It cannot be directly related to a pole in the analytic continuation and thus interpreted as a collective mode².

c. BCS regime When going to the BCS regime (Fig. 4), the low- q damping of the collective mode increases (as prescribed by (10)) such that the resonance fades out quicker. The skewness of the resonance (which no longer fits to a Lorentzian function [17]) is also larger, such that the peak maximum is displaced from $\omega_{\mathbf{q}}$. The sharp peak which appears at high q near the continuum lower-edge is also much less intense than in the strong-coupling regime.

² We note that a solution of (3) still exists at $q > 3.29$ where the red and green lines of Fig. 2 stop. Having a negative damping rate $\gamma_{\mathbf{q}} < 0$, this solution is not in the “physical sector” (defined in the introduction of section IV) and can hardly be interpreted as a collective mode.

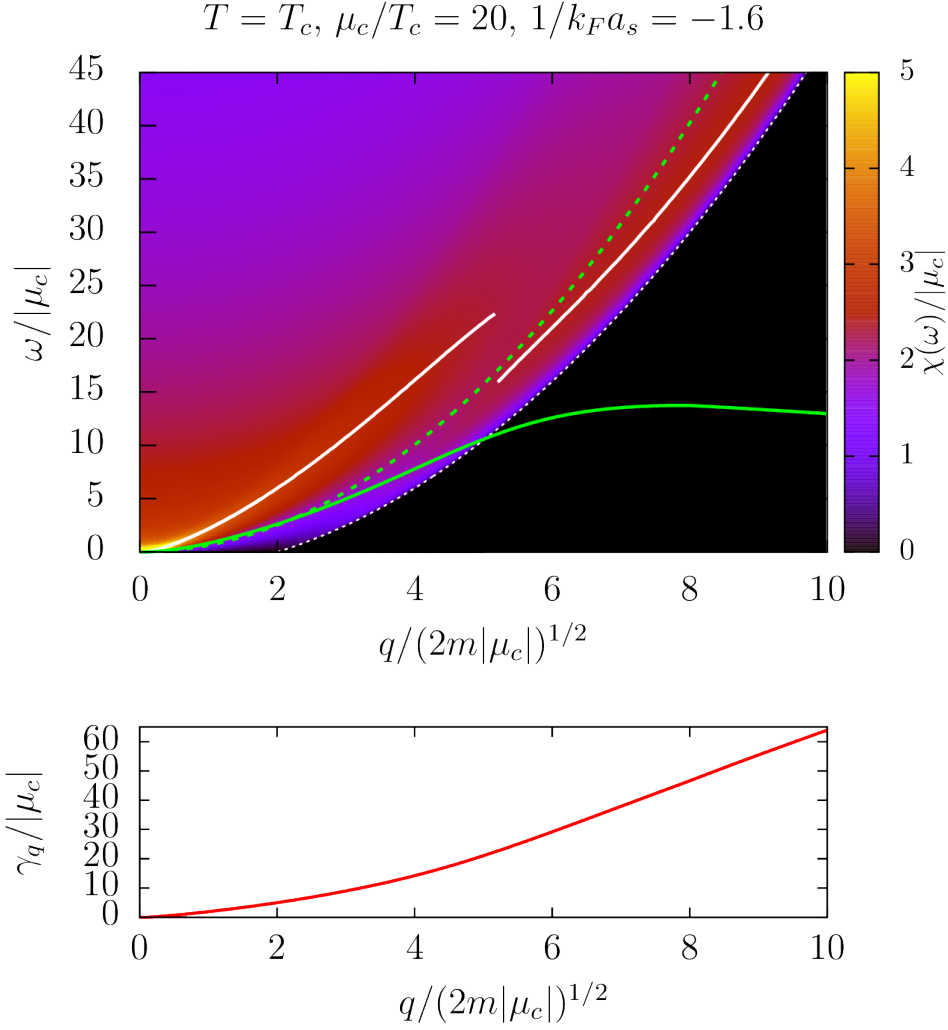


FIG. 4: (Upper panel) The pair spectral function $\chi(q, \omega + i0^+)$ in the BCS regime ($1/k_F a \simeq -1.6$). The curves superimposed to the color plot are the same as on Fig. 2. Note the discontinuity of the location of the spectral function maximum, when the sharp peak appears near the continuum edge. (Lower panel) The damping rate $\gamma_{\mathbf{q}}$.

d. BEC regime Fig. 5 shows the spectral function in the BEC regime ($1/k_F a \simeq 1.0$ and $\mu/T_c = -0.5$). In this regime a Dirac peak corresponding to an undamped collective mode (red solid line) exists below the lower-edge of the continuum $\omega_0(q)$ (dashed white line). The spectral function in the continuum is smooth with a shallow maximum near the continuum edge. At large q , the eigenenergy $\omega_{\mathbf{q}}$ tends from below to the threshold energy $\omega_0(q)$.

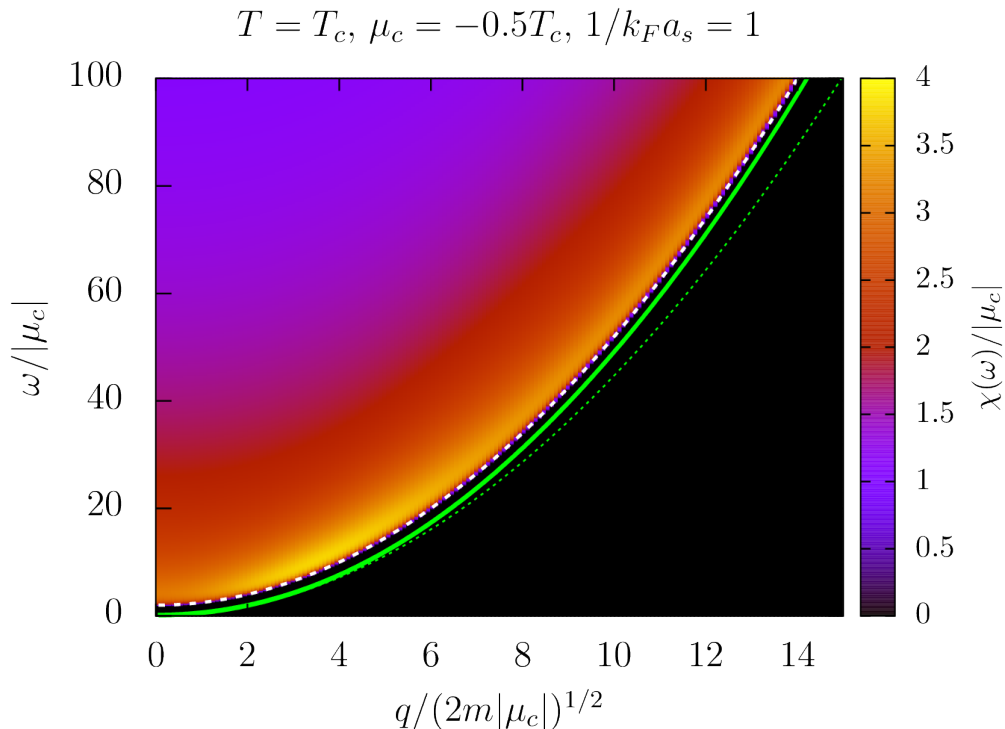


FIG. 5: The pair spectral function $\chi(q, \omega + i0^+)$ is plotted in colors as a function of q and ω at $T = T_c$ and in the BEC regime ($1/k_F a_s \simeq 1.0$ and $\mu_c/T_c = -0.5$). The eigenfrequency of the collective mode $\omega_{\mathbf{q}}$ (red solid line), its low- q expansion (dashed red) and the lower-edge of the continuum $\omega_0(q)$ (dashed white) are superimposed to the color plot.

IV. COLLECTIVE EXCITATIONS BELOW THE TRANSITION TEMPERATURE

In this section we perform a complete study of the solutions of the dispersion equation (3), at arbitrary momentum, in the whole temperature range $0 < T < T_c$, and both below (Sec. IV B) and above (Sec. IV C) the pair-breaking continuum threshold. Generally, collective excitations can be reliably attributed to known types, such as Anderson-Bogoliubov (phase), pair-breaking (amplitude) modes, or the pairing mode found at T_c only in limiting cases (such as $q \rightarrow 0$, $T \rightarrow 0$ or $T \rightarrow T_c$). At temperatures away from 0 and T_c , the spectral function may have a non-trivial structure with more than one maximum, and correspondingly two (or more) interfering poles [15] in the analytic continuation. This motivates an exhaustive cartography of all poles of the analytic continuation, as a basis of a rigorous

classification of all collective phenomena.

The analytic continuation of the GPF propagator in the general case raises subtle questions, which require a careful analysis. As soon as several angular points appear on the real axis, they determine several analyticity intervals, which open distinct windows for the analytic continuation (see Fig. 6). A straightforward and “naive” way to determine complex roots of Eq. (3) would be to choose a piecewise rule for the analytic continuation, where the branch cut on the real axis is converted to vertical branches attached to each branching point and extending to the lower-half complex plane. However, other continuation schemes are possible, as described in Refs. [15, 17–19]. We can in particular extend the analytic continuation through a chosen window to the entire lower half of the complex plane (see, e. g., Fig. 2 of Ref. [17]). As a result, each window can provide poles whose real part is outside the continued interval of analyticity.

Mathematically, the analytic continuation of \mathbb{M} is defined in infinite layers of Riemann sheets obtained by winding around the branching points between which the continuation is performed. Ref. [22] showed for instance that a monodromic infinity of poles are obtained at $T = 0$ by winding around the point $\omega = 2\Delta$. This being said, poles lying far away from the original branch cut have a smaller impact on the response function, and thus little physical significance. For this reason, we restrict our exploration of the analytic continuation to the “physical sector” defined as the fourth quadrant ($\text{Re } z > 0$ and $\text{Im } z < 0$) of the first Riemann sheet³. However one should keep in mind that solutions initially belonging to “unphysical” sectors of the analytic continuation (such as *e.g.* the quadrant $\text{Re } z < 0$, $\text{Im } z < 0$) may eventually enter the physical sector [15, 19] as q and T vary. Or, vice-versa, poles of the physical sector may eventually leave it.

A. Angular points and intervals for the analytic continuation

The analytic continuation is performed using the standard scheme. Consider a function F of the complex variable z having a branch cut on the real axis $z = \omega$ and introduce the associated spectral density,

$$\rho_F(\omega) = -\lim_{\delta \rightarrow 0} \frac{F(\omega + i\delta) - F(\omega - i\delta)}{2\pi i}. \quad (20)$$

³ Without loss of generality, we study the spectral functions only at $\omega > 0$.

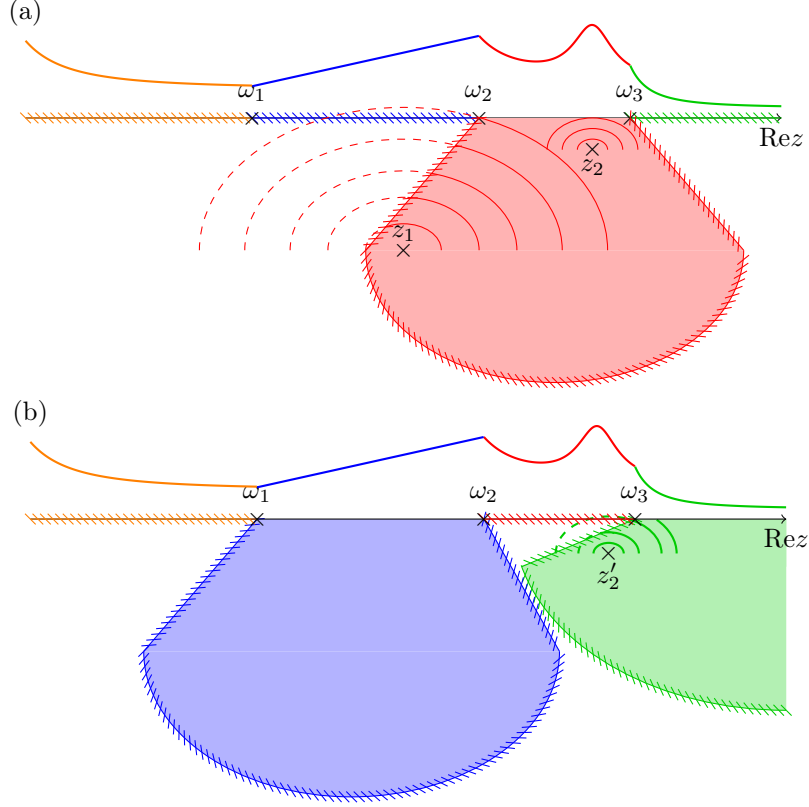


FIG. 6: **Analytic continuations of a response function with multiple angular points.**

The analytic continuation of χ from the interval $[\omega_2, \omega_3]$ to the lower-half-complex plane (red area on pannel (a)) has two poles in z_1 and z_2 . The first pole has a real part comprised between ω_1 and ω_2 and gives rises to a resonance in $\chi(\omega)$ (visible to the right of the red solid curve). This pole has a counter-part z_1' in the analytic continuation through $[\omega_3, +\infty[$ (green area in (b)), such that the resonance peak is only slightly broken in ω_3 and appears to extend beyond it. This contrasts with the pole z_2 , which has no counter-part in the continuation through $[\omega_1, \omega_2]$ (blue area in (b)). The “resonance” then abruptly terminates in ω_2^+ , such that only its upper tail is visible in $\chi(\omega)$ (to the left of the interval $[\omega_2, \omega_3]$).

The spectral density $\rho_F(\omega)$ is in general analytic on the real axis except at most on a finite number of points. It can thus be analytically continued from any chosen interval between these points to the lower complex half-plane. The analytic continuation $F^{(I)}(z)$ of $F(z)$ from upper to lower complex half-plane and through the interval $I \subset \mathbb{R}$ where ρ_F is analytic

then reads:

$$F^{(I)}(z) = \begin{cases} F(z), & \text{Im } z > 0, \\ F(z) - 2\pi i \rho_F^{(I)}(z), & \text{Im } z < 0, \end{cases} \quad (21)$$

where $z \rightarrow \rho_F^{(I)}(z)$ is the analytic continuation of $\rho_F(\omega)$ from the interval I to the lower complex half-plane.

The angular points of the spectral density mark a change in the configuration (usually in the number of connected components) of the resonant wavevectors for one of the two resonance conditions:

$$E_{\mathbf{k}-\frac{\mathbf{q}}{2}} + E_{\mathbf{k}+\frac{\mathbf{q}}{2}} = \omega, \quad \left| E_{\mathbf{k}-\frac{\mathbf{q}}{2}} - E_{\mathbf{k}+\frac{\mathbf{q}}{2}} \right| = \omega \quad (22)$$

where $E_{\mathbf{k}} = \sqrt{\xi_{\mathbf{k}}^2 + \Delta^2}$ is the BCS excitation energy and $\xi_{\mathbf{k}} = k^2 - \mu$ the free-fermion energy (in this section we set $\hbar = k_B = 2m = 1$, which is equivalent to working in Fermi units ϵ_F and k_F respectively for energies and wavevectors), and we assume $\omega > 0$ without loss of generality. The angular points obtained from the first resonance condition are essential for the analytic continuation both for zero and nonzero temperatures. They affect the “particle-particle” terms in the matrix elements. The angular points obtained from the second resonance condition affect the “particle-hole” terms and must be taken into account only when $T \neq 0$.

As described in Ref. [17], there exist three frequencies corresponding to angular points in the zero temperature case. The frequency ω_1 is the boundary of the pair-breaking continuum,

$$\omega_1 = \begin{cases} 2\Delta, & \mu - q^2/4 \geq 0, \\ 2\sqrt{(\mu - q^2/4)^2 + \Delta^2}, & \mu - q^2/4 < 0. \end{cases} \quad (23)$$

The frequency $\omega_3 = 2\sqrt{(\mu - q^2/4)^2 + \Delta^2}$ is the energy of the BCS pair $E_{\mathbf{k}-\frac{\mathbf{q}}{2}} + E_{\mathbf{k}+\frac{\mathbf{q}}{2}}$ at $k = 0$. For $\mu - q^2/4 < 0$, these frequencies coincide $\omega_1 = \omega_3$.

The other angular point frequencies correspond to local minima/maxima of the energies $E_{\mathbf{k}-\frac{\mathbf{q}}{2}} \pm E_{\mathbf{k}+\frac{\mathbf{q}}{2}}$ at $\cos \theta_{\mathbf{k},\mathbf{q}} = \pm 1$, where $\theta_{\mathbf{k},\mathbf{q}}$ is the angle between \mathbf{k} and \mathbf{q} . They are provided by solutions of the equations

$$\frac{\partial \left(E_{\mathbf{k}-\frac{\mathbf{q}}{2}} + E_{\mathbf{k}+\frac{\mathbf{q}}{2}} \right)}{\partial k} = 0, \quad (24)$$

$$\frac{\partial \left(E_{\mathbf{k}-\frac{\mathbf{q}}{2}} - E_{\mathbf{k}+\frac{\mathbf{q}}{2}} \right)}{\partial k} = 0, \quad (25)$$

which lead to the equation for $\varepsilon \equiv k^2$, unique for both particle-particle and particle-hole angular points,

$$\begin{aligned}
& 256\varepsilon^4 - 256(q^2 + 4\mu)\varepsilon^3 + 32(8q^2\mu + 3q^4 + 48\mu^2 + 24\Delta^2)\varepsilon^2 \\
& + 16\left(8\Delta^2(5q^2 - 8\mu) - (q^2 + 4\mu)(q^2 - 4\mu)^2\right)\varepsilon \\
& + (q^2 - 4\mu)\left((q^2 - 4\mu)^3 + 16\Delta^2(3q^2 - 4\mu)\right) = 0.
\end{aligned} \tag{26}$$

This equation provides up to four (restricted by the additional condition $\varepsilon > 0$) frequencies. They can be classified as $(\omega_{2s,1}, \omega_{2s,2})$ which satisfy (24), and $(\omega_{2a,1}, \omega_{2a,2})$ which satisfy (25). The ordering of the frequencies is chosen in such a way that $\omega_{2s,1} < \omega_{2s,2}$ and $\omega_{2a,1} > \omega_{2a,2}$. The chosen ordering for $(\omega_{2s,1}, \omega_{2s,2})$ coincides with the selection of the root for ω_2 in Ref. [19]. In this classification, ω_2 of the preceding work [17] coincides with $\omega_{2s,1}$. An example of these real solutions, together with ω_1 and ω_3 , is shown in Fig. 7 for $\mu/\Delta|_{T=0} = 5$, that corresponds to the inverse scattering length $1/k_F a_s \approx -1.0577$. The temperature is here $T = 0.5T_c$.

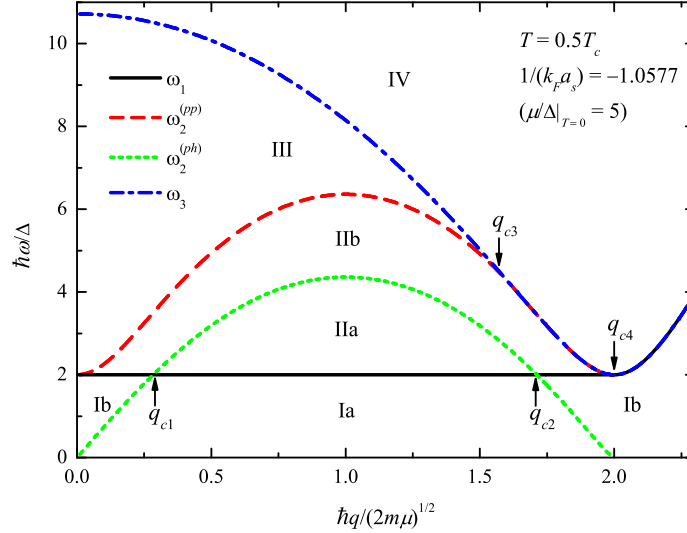


FIG. 7: Angular-point frequencies for the analytic continuation of the GPF matrix elements for $1/k_F a_s \approx -1.0577$ and $T = 0.5T_c$. The areas between curves determine intervals for the analytic continuation as described in the text. The arrows show values of momentum q_{c1}, \dots, q_{c4} at which different angular-point frequencies coincide.

After selecting physically reasonable roots from the aforesaid four ones, we find that two frequencies $\omega_{2s,1} \equiv \omega_2^{(pp)}$ and $\omega_{2a,1} \equiv \omega_2^{(ph)}$ correspond, respectively, to the particle-particle and particle-hole angular points. The particle-particle angular point frequency $\omega_2^{(pp)}$

is important both at zero and nonzero temperatures and is described in Ref. [17]. The particle-hole angular point frequency $\omega_2^{(ph)}$ contributes only at $T \neq 0$. Particularly, the frequency $\omega_2^{(ph)}$ behaves linearly at small momentum, thus affecting phononic modes. In the small-momentum limit, the particle-hole angular point frequency asymptotically tends to $c_b q$, where c_b is the boundary sound velocity determined in Ref. [15] and corresponding to the opening/closing of a decay channel in the part of the BCS excitation branch at $k < \sqrt{2m\mu}$.

For any given q , intervals between different angular-point frequencies determine windows for the analytic continuation. Consequently, they are described by the areas in Fig. 7 between different curves. The classification of the windows in the figure, performed by Roman numbers, extends their zero-temperature classification of Ref. [19] to nonzero temperatures due to the appearance of the particle-hole angular point frequency $\omega_2^{(ph)}$. Below the pair-breaking continuum, this leads to the subdivision of the interval I to two intervals Ia and Ib, respectively below and above $\omega_2^{(ph)}$. We introduce here several critical values of q at which different angular-point frequencies cross or touch each other. The particle-hole angular point frequency $\omega_2^{(ph)}$ may cross the pair-breaking continuum edge ω_1 , as shown in the figure. In this case, also the interval II is subdivided to two intervals IIa and IIb, as shown in the figure, and we denote q_{c1} and q_{c2} the crossing points. Therefore at nonzero temperatures the angular point $\omega_2^{(ph)}$ is important for both phononic and pair-breaking collective excitations. This is a non-trivial difference between the zero-temperature and nonzero-temperature cases. As can be seen from the figure, the particle-particle angular point frequency $\omega_2^{(pp)}$ exists for q smaller than a critical value $q \equiv q_{c3}$, above which it coincides with ω_3 . Finally, the pair-breaking continuum edge and ω_3 become equal to each other at $q > q_{c4}$, where $q_{c4} \equiv 2\sqrt{2m\mu}$. In the following subsection, we index the obtained solutions of Eq. (3) according to the classification of intervals described in Fig. 7: for exemple $\omega_{\text{IIb}}^{(i)}$ will be the i -th root of $\det \mathbb{M}$ found in the analytic continuation through window IIb.

When analytic continuations through two adjacent intervals separated by an angular point have drastically different analytic structures, the shape of the spectral function abruptly changes at the angular point, with for instance the sudden termination of a resonance peak (see schematically the blue and red intervals in Fig. 6). At low temperature, the lower edge ω_1 of the pair-breaking continuum is such a sharp angular point dividing the frequencies into low- and high-energy regions with much different physics. On the contrary, adjacent

intervals may yield similar analytic structures, with poles in particular lying close to one another (as was the case in Ref. [15] for phononic poles computed from above or below $\omega_2^{(\text{ph})}$, see schematically the green and red intervals in Fig. 6). In this case, the spectral function, despite a small kink at the angular point maintains an overall similar shape on both sides of it, and the poles in different windows can be attributed to the same physical phenomenon. In what follows, we consider poles belonging to different continuation windows to be physically equivalent when their energy separation is smaller than their inverse lifetime, making them nearly indistinguishable on the real axis.

The equivocality of the complex eigenfrequencies shows the limits to the concept of quasiparticle. In a system of interacting particle, this concept is an *approximation* used to grasp the most stringent features of a continuous spectrum. Whereas interpreting a single Lorentzian resonance in terms of a complex pole is straightforward, even for broad resonances, doing so in case of multiple resonances, or of an asymmetric, non Lorentzian, resonance is less obvious. In these cases, the knowledge of the analytic continuation can help distinguish between peaks that can be related to complex poles (although they may be distorted by the continuum background [17]), and thus interpreted as resonances, and peaks which only correspond to a continuum edge.

B. Phononic-like collective excitations

Frequencies and damping factors for phononic collective excitations in the long-wavelength limit at nonzero temperatures have been calculated in Ref. [15] using the analytic continuation of the inverse GPF propagator expanded at small q . Contrary to a naive expectation of two branches for a complex field with a modulus and a phase, the spectrum of collective excitations at nonzero temperature can contain more than two branches, due to the additional degrees of freedom provided by the normal component. As shown in Ref. [15], the spectrum contains in particular two phononic branches, reminiscent of the first and second sound modes of the hydrodynamic theory of superfluids. Here, we extend the study of those two branches to finite momentum. We recall that at zero temperature the only phononic branch (identified as hydrodynamic first sound) tends to the pair-breaking continuum threshold, either at a finite wavevector q_{sup} in the BCS regime, or asymptotically in $q = +\infty$ in the BEC regime. At temperatures low compared to T_c [13], and in fact in a rela-

tively wide temperature range below T_c , the dispersion shows qualitatively the same features as in the zero-temperature case, and the damping rate behave as in Ref. [13] (falling off to 0 both when $q \rightarrow 0$ and when the branch approach the pair-breaking continuum threshold).

We are interested here rather in the regime of T close to T_c where the second branch enters the physical sector (coming from the third quadrant of the complex plane). We identify two remarkable phenomena in the finite q behavior of the two branches. First, the mechanism which confines the phononic branch below the pair-breaking continuum at $T = 0$ is lifted here because of the presence of the particle-hole scattering channel. One of the two branches thus enters the pair-breaking continuum at large q (while the other leaves the physical sector). Second, in the BCS regime, the two branches exchange their high- q behavior at some remarkable temperature: while at low T , the “first branch” (the one which evolves from the $T = 0$ first sound) reaches the continuum, at temperatures close to T_c , it is instead the second branch. Separating the two scenarios is an exceptional temperature T_{ex} where the two branches exactly meet (both in real and imaginary part) at an exceptional momentum q_{ex} . We note that this section adopts a rather theoretical perspective on the collective modes, as the phenomena we describe are hardly observable on the spectral functions.

In Fig. 8, we consider⁴ collective excitations at $1/(k_F a_s) = 0$ and two different temperatures to illustrate the changes taking place when approaching T_c . Following the convention of Ref. [15], we call here the “first branch” ($z_I^{(1)}$) the one whose sound velocity continuously evolves to the velocity of first sound at $T = 0$. In the BCS regime ($1/k_F a \lesssim 0.155$, see the discussion in section VI. B. 1. in [15]), this first branch always has a larger sound velocity, *i.e.* $\omega_I^{(1)} > \omega_I^{(2)}$ when $q \rightarrow 0$ and for all T . At $1/k_F a > 0.155$, it is rather the imaginary part

⁴ We note that employing window Ia or Ib for the analytic continuation results *a priori* in distinct solutions. However, the energy mismatch introduced by the change of window remains small (in particular smaller than the imaginary part of the poles) at all momenta. For this reason, we show results only for the window which seems best adapted to follow the dispersion of the branch. In the case when $\max_q \omega_2^{(ph)} < \omega_1$, the interval Ia is restricted by the inequality $q < q_{c4} \equiv 2\sqrt{2m\mu}$, while the interval Ib is not restricted, see Fig. 7. In this case we show results only for window Ib. When $\max_q \omega_2^{(ph)} > \omega_1$, interval Ib disappears at $q_{c1} < q < q_{c2}$, so interval Ia is preferable in this figure. Below, poles of the GPF propagator are used for an analytic simulation of spectral functions. The selection of appropriate poles is automatically determined by an interval between two neighboring angular points for the frequency argument ω of the spectral function. This completely resolves the question of a choice of a preferable interval for poles to reproduce the spectral function for a given ω .

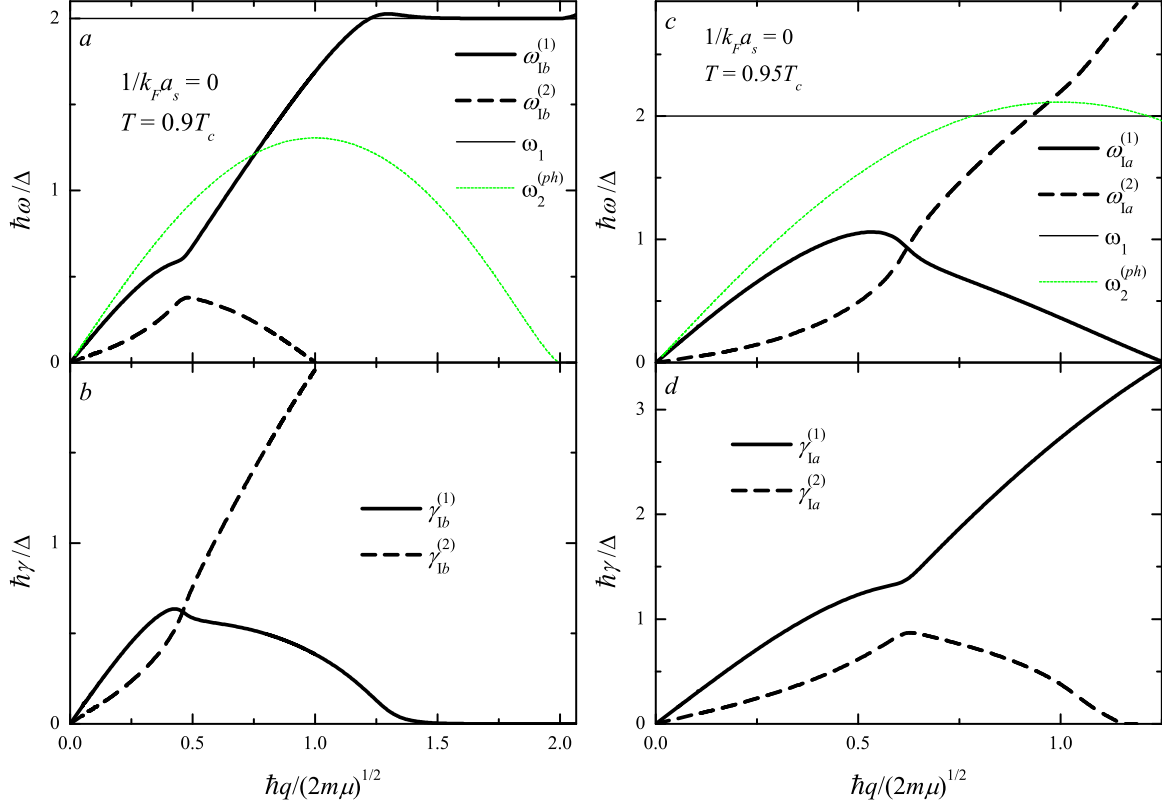


FIG. 8: Momentum dispersion of the frequency (*a*, *c*) and damping (*b*, *d*) of collective modes obtained using the analytic continuation in frequency intervals below the pair-breaking continuum at $1/(k_F a_s) = 0$ with $T/T_c = 0.9$ (*a*, *b*) and $T/T_c = 0.95$ (*c*, *d*). The classification of intervals follows the scheme described in Fig. 7. Heavy solid and dashed curves show the solutions corresponding, respectively, to the first and second pole of the GPF propagator. Thin curves indicate the angular-point frequencies ω_1 (the pair-breaking continuum edge) and $\omega_2^{(ph)}$ (the particle-hole angular point frequency).

which distinguishes the two modes: the first branch always has (at all T and this time also all q) a lower imaginary part: $\gamma_I^{(1)} < \gamma_I^{(2)}$.

For larger momenta, the phononic branches behave strongly nonlinearly and non-monotonically. For $T = 0.9T_c$, the second eigenfrequency passes a maximum and then goes down. The first eigenfrequency continues to increase after its linear start eventually crossing the pair-breaking continuum edge ω_1 . When the branch reaches the pair-breaking continuum edge, its damping diminishes (as in the low temperature case [13]), while the other solution becomes overdamped. Although the phononic branch no longer fulfills the

piecewise rule when it is above ω_1 , this penetration in the continuum suggests the presence of an observable resonance inside the pair-breaking continuum, whose lower tails extends to the phononic intervals Ia and Ib. We will show below that this resonance is nothing else than the developing pairing mode $z^{(T_c)}$.

Remarkably, the high- q behavior of the first and second poles is switched when temperature increases from $T = 0.9T_c$ to $T = 0.95T_c$. While at $T = 0.9T_c$ the frequency of the second pole is always below that of the first pole, at $T = 0.95T_c$ its frequency is lower than that of the first pole at small momentum, but larger at higher q , penetrating into the pair-breaking continuum. This demonstrates an avoided crossing of complex poles when varying temperature. We remind that an analogous phenomenon was observed in Ref. [15] for complex sound velocities. The two complex poles behave as repulsive particles in the complex z plane with one of the parameters $(q, T, 1/a_s)$ playing the role of time. In between the left and right panels of Fig. 8, there exists a specific temperature T_{ex} corresponding to a precise “head-on collision” of the two poles in an exceptional point (q_{ex}, T_{ex}) , where crossing and anticrossing cannot be distinguished. At $1/a_s = 0$ this exceptional point lies at $q_{ex} \approx 0.556\sqrt{2m\mu}$ and $T_{ex} \approx 0.933T_c$. When varying the interaction strength, both T_{ex} and q_{ex} increase towards the BCS regime (with T_{ex} in particular tending to T_c when $1/k_F a \rightarrow -\infty$). q_{ex} eventually vanishes at $1/k_F a \approx 0.155$ when the sound velocities show an exact crossing [15]. Then, at $1/k_F a > 0.155$ the situation is simpler: the second root always has a larger imaginary part (at all q and all temperature), and never penetrates the pair-breaking continuum. In this regime, the second root thus has little physical significance (even when its sound velocity is above that of the first root, as this happens above a crossing temperature).

We note the interesting mathematical properties of the exceptional point (q_{ex}, T_{ex}) where the two roots are equal and thus indistinguishable. It constitutes a second order branching point of the functions $(q, T) \mapsto z_I^{(1)}(q, T)$ and $(q, T) \mapsto z_I^{(2)}(q, T)$: close contours with a winding number of ± 1 around (q_{ex}, T_{ex}) exchange $z_I^{(1)}$ and $z_I^{(2)}$. Anticipating on the discussion of section IV D, we also note a divergence of the residues of both poles at the exceptional point.

C. Collective excitations provided by intervals inside the pair-breaking continuum

1. Pair-breaking branch

In this paragraph, a special attention is paid to the finite-temperature behavior of the pair-breaking collective excitations, treated previously at $T = 0$ in Ref. [17]. According to the classification of intervals for the analytic continuation in Fig. 7, there exist two windows relevant for the pair-breaking branch of collective excitations: IIa and IIb. Since the solutions in either continuation are never too far apart⁵ (their frequency separation $|\omega_{\text{IIb}} - \omega_{\text{IIa}}|$ in particular is much lower than their damping rate, which makes them indistinguishable on the real axis), we always use window IIb which provides solutions at all momenta (whereas window IIa is limited to $q_{c1} < q < q_{c2}$).

In Fig. 9, the frequency and the damping factor are plotted as functions of momentum for different temperatures with the same value of the inverse scattering length $1/k_F a_s \approx -1.0577$ as above in Fig. 7. This value of the inverse scattering length is in the BCS regime. For comparison, the results of the small-momentum expansion developed in Ref. [18] have been added to the figures (short-dashed and dot-dashed curves). As can be seen from Fig. 9, the quadratic series expansion is close to the result of the full calculation for $q \lesssim 0.02\sqrt{2m\mu}$. It cannot capture however a non-monotonic behavior of the dispersion of pair-breaking modes at larger q . Conversely, the damping factor $\gamma_{\mathbf{q}}$ monotonically rises when increasing q . For $\hbar q \gtrsim \sqrt{2m\mu}$, the pair-breaking mode frequency shifts to higher energy in the continuum, becoming strongly damped. This behavior is qualitatively common for the zero and non-zero temperatures.

For relatively low temperatures, the momentum dependence of the pair-breaking mode frequency and damping is qualitatively close to that at $T = 0$ reported in Ref. [17]. For higher temperatures, however, a qualitative difference appears. At sufficiently high temperatures, as we can see from Fig. 9 (a), the mode frequency exhibits oscillations just before moving to the overdamped regime. Those oscillations are not visible in the spectral functions, and their magnitude is relatively small with respect to damping. Hence they are not

⁵ We show both solutions (a , b) only once in the inset of Fig. 9, to demonstrate that they are indeed close to each other within the linewidth determined by the damping factor. In other figures, we avoid duplication of physically equivalent solutions.

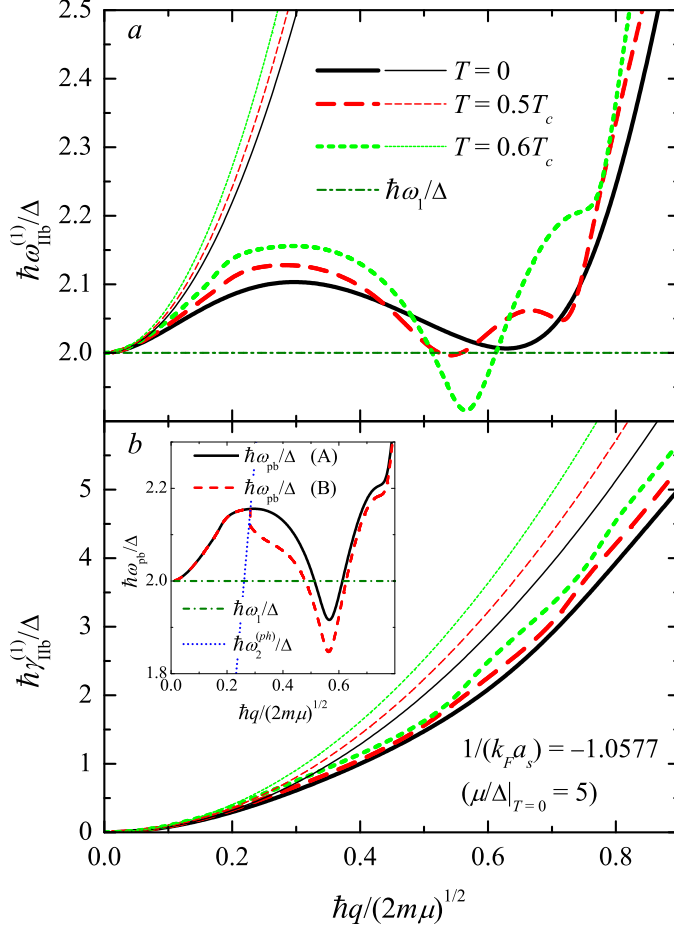


FIG. 9: Frequency $\omega_{\text{Ib}}^{(1)}(q)$ (panel *a*) and damping factor $\gamma_{\text{Ib}}^{(1)}(q)$ (panel *b*) of the pair-breaking collective excitations as a function of momentum at different temperatures for $1/k_F a_s \approx -1.0577$, which corresponds to $\mu/\Delta|_{T=0} = 5$. Thin curves show the low- q expansion, and heavy curves are results of the full calculation. The dot-dashed line indicates the pair-breaking continuum edge. *Inset*: the frequency at $T = 0.6T_c$ calculated using different windows for the analytic continuation. The dotted curve is the angular-point frequency $\omega_2^{(ph)}$.

an observable phenomenon, rather a mathematical peculiarity of the analytic continuation.

At unitarity, the quadratic start of pair-breaking mode eigenfrequency is slower, as can be seen from Fig. 10. There (and for stronger couplings), the sign of the dispersion is negative at low q , so that the frequency goes to the “forbidden” area $\omega_{\text{II}}^{(1)} < \omega_1$, when using the analytic continuations through both window IIa and IIb. At large q , the dispersion becomes non-monotonic. For sufficiently high momentum, the eigenfrequencies can therefore appear above the pair-breaking continuum, being however substantially damped. As found in [17],

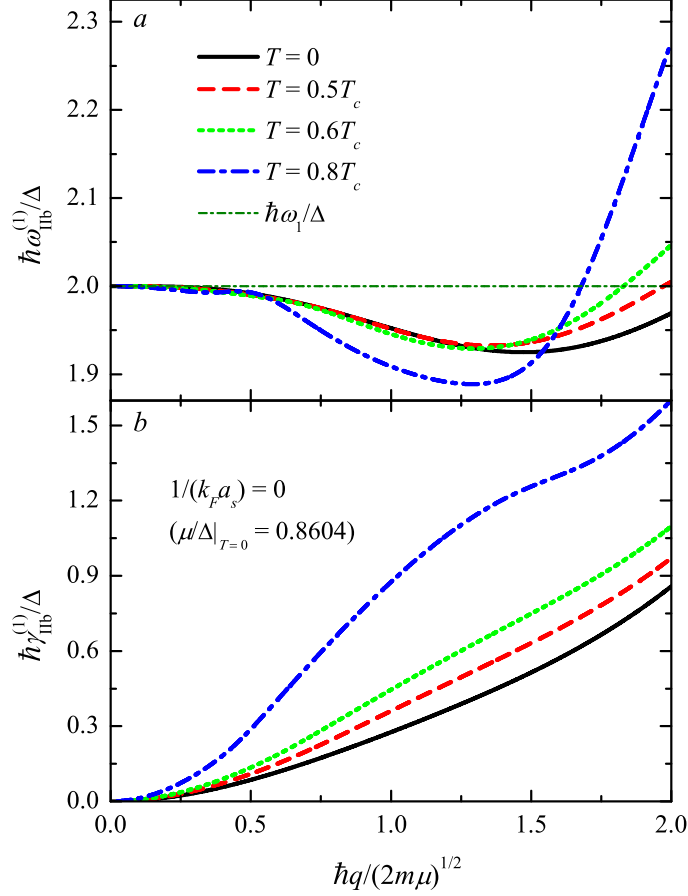


FIG. 10: Frequency $\omega_{\text{Ib}}^{(1)}(q)$ (panel *a*) and damping factor $\gamma_{\text{Ib}}^{(1)}(q)$ (panel *b*) of the pair-breaking collective excitations as a function of momentum at different temperatures for $1/k_F a_s = 0$, which corresponds to $\mu/\Delta|_{T=0} \approx 0.8604$. Thin curves show the low- q expansion, and heavy curves are results of the full calculation. The dot-dashed line indicates the pair-breaking continuum edge.

the damping of pair-breaking modes at unitarity is smaller than in the BCS regime.

Fig. 11 show the temperature dependence of the frequency and damping of pair-breaking collective excitations for $1/k_F a_s \approx -1.0577$ at the particular value of momentum $q = 0.1\sqrt{2m\mu}|_{T=0}$. Also 2Δ has been plotted at the same graph. In panel (*b*) of the figure, we plot the inverse quality factor $\gamma_{\mathbf{q}}/\omega_{\mathbf{q}}$ as a function of T/T_c . The results of the full calculation within the present arbitrary-momentum method are compared with the results of the small-momentum expansion [18]. As can be seen from Fig. 11, the low-momentum expansion agrees well with the full calculation at a relatively small momentum $q = 0.1\sqrt{2m\mu}|_{T=0}$ everywhere except in a temperature range close to the transition temperature, where the long-wavelength expansion (limited to $q \ll 1/\xi_{\text{pair}}$) is no longer valid for the selected value

of q . The small-momentum expansion exhibits a divergence for both the frequency and the damping factor when T tends to T_c . On the contrary, the full finite-momentum calculation predicts finite values for the frequency and the damping factor in the limit $T \rightarrow T_c$.

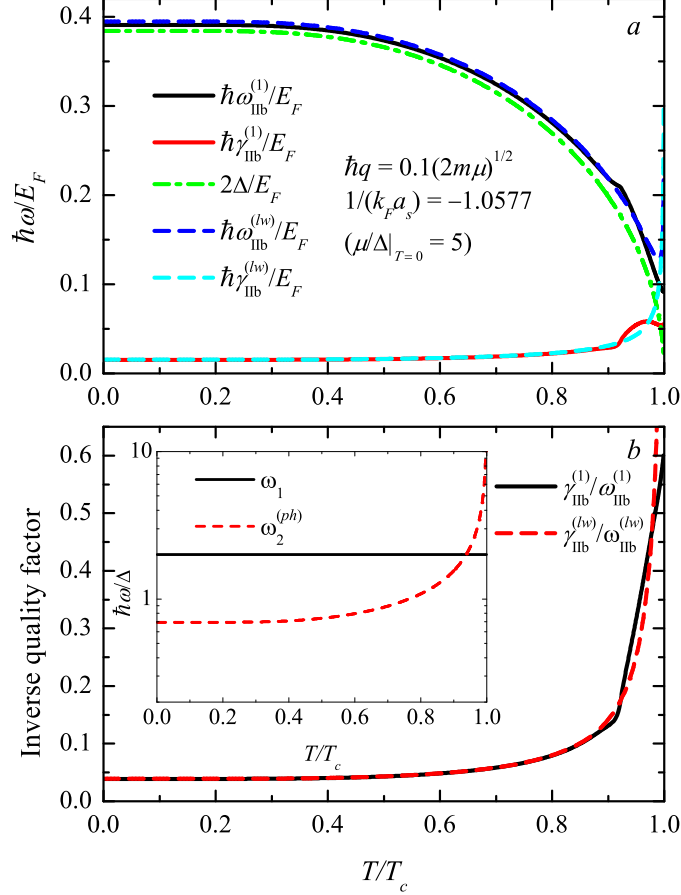


FIG. 11: (a) Temperature dependence of the frequency and damping of pair-breaking collective excitations with momentum $q = 0.1\sqrt{2m\mu}|_{T=0}$ for $1/k_F a_s \approx -1.0577$. Solid black and red curves show, respectively the frequency and the damping factor as functions of T/T_c . Dashed curves represent the results of the small- q expansion [18]. The dot-dashed green curve shows 2Δ . (b) The inverse quality factor $\gamma_{\mathbf{q}}/\omega_{\mathbf{q}}$ calculated within the full calculation and the low-momentum expansion. *Inset*: temperature dependence of the boundary frequencies ω_1 (solid curve) and $\omega_2^{(ph)}$ (dashed curve).

In the inset to Fig. 11, we plot the particle-particle and particle-hole angular-point frequencies. For $q = 0.1\sqrt{2m\mu}|_{T=0}$, they cross each other at a temperature relatively close to T_c . This explains the fast non-monotonic behavior of the eigenfrequency and the damping factor at T close to T_c in Fig. 11 (a) and the failure of the long-wave length expansion,

limited near T_c to $\omega_2^{(ph)} < \omega_1$, that is $q^2 \ll \Delta^2/\mu$.

The temperature dependence of the eigenfrequency and the damping factor for a higher momentum $q = 0.3\sqrt{2m\mu|_{T=0}}$ is plotted in Fig. 12. The difference between the results of the full-momentum calculation and the small- q expansion is here larger than in the case of smaller momentum, but the temperature dependence remains qualitatively the same although it is smoother. The inset to Fig. 12 shows plot the particle-particle and particle-hole angular-point frequencies. For $q = 0.3\sqrt{2m\mu|_{T=0}}$, as compared with the result shown in Fig. 11, this crossing is relatively smooth and at a lower temperature, so that we do not observe a fast change of frequencies and damping factors in Fig. 12.

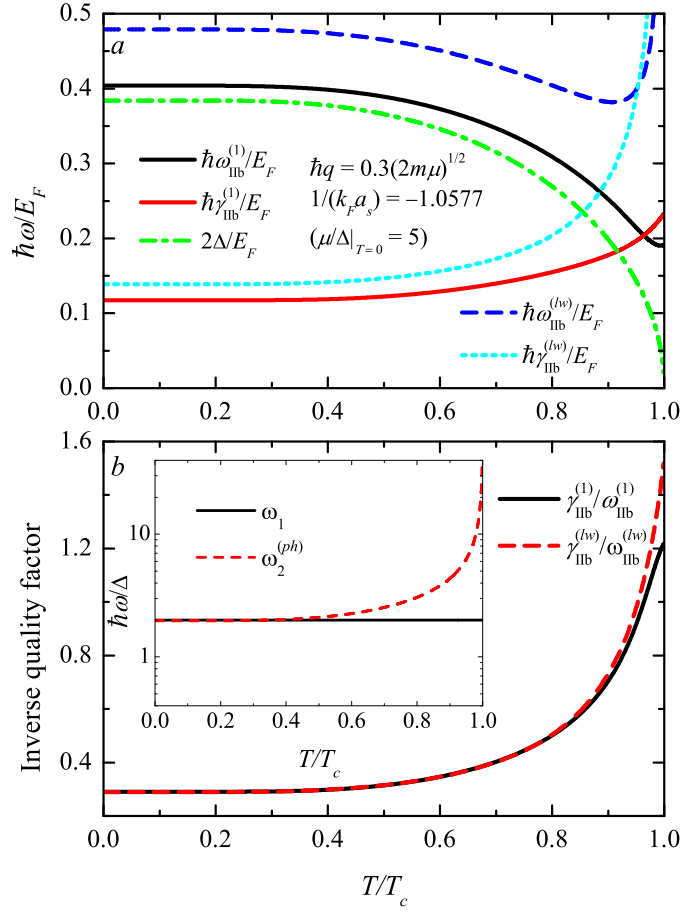


FIG. 12: Temperature dependence of the frequency, damping and the inverse quality factor of pair-breaking collective excitations with momentum $q = 0.3\sqrt{2m\mu|_{T=0}}$ for $1/k_F a_s \approx -1.0577$. The notations are the same as in Fig. 11.

2. Pole-doubling near T_c and interplay with branches in windows III and IV

In this subsection, we consider the parallel evolution of all collective modes obtained using the analytic continuation through intervals IIa, IIb, III and IV. These intervals are positioned above the pair-breaking continuum such that the obtained solutions take into account both particle-particle and particle-hole scattering processes. In Fig. 13, we show their dispersion relations at unitarity and both $T/T_c = 0.9$ and $T/T_c = 0.95$.

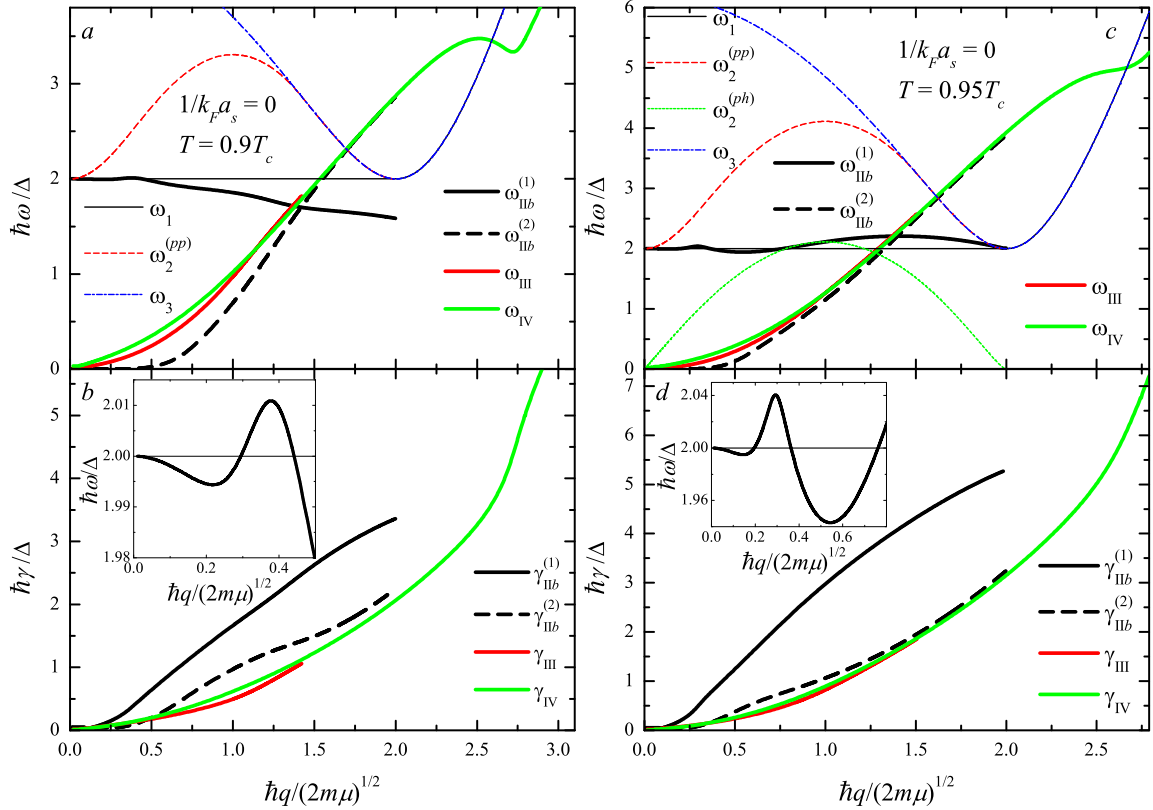


FIG. 13: Momentum dependence of eigenfrequencies (a , c) and damping factors (b , d) for collective excitations determined using the analytic continuation through intervals positioned above the pair-breaking continuum edge. Here, $T = 0.9T_c$ (a , b), $T = 0.95T_c$ (c , d), with $1/(k_F a_s) = 0$. Black heavy solid and dashed curves represent the solutions corresponding, respectively, to the first and second pole of the GPF propagator resolved through window II (here window IIb is used). Red and green solid lines show the (unique) pole in respectively window III and IV. Thin curves show the angular-point frequencies ω_1 (the pair-breaking continuum edge), $\omega_2^{(pp)}$ (the particle-particle angular point frequency), $\omega_2^{(ph)}$ (the particle-hole angular point frequency), and ω_3 . *Insets*: the low-momentum part of the pair-breaking mode frequency scaled for a better resolution.

Remarkably, when T is sufficiently close to T_c a new pole (shown by the black dashed curves on Fig. 13) appears in the physical region ($\text{Re} z > 0$ and $\text{Im} z < 0$) of the window IIa and/or IIb. This is quite reminiscent of the pole-doubling already observed (in section IV B and Ref. [15]) in the phononic windows (Ia and Ib). At low- q , the eigenfrequency of this pole tends to 0 (in contrast with the pair-breaking “Higgs” mode (black solid line), whose eigenfrequency tends to 2Δ) and at $\hbar q \approx \sqrt{2m\mu}$ it lies in the interval $[\omega_1, \omega_2]$ such that it fulfills the piecewise rule (with a damping rate lower than that of the first pole). This second pole thus seems to correspond to a physically observable resonance when the momentum is sufficiently large. In fact we show on Fig. 14 that when $T \rightarrow T_c$, and for $1/\xi_{\text{pair}} \ll q$, this pole tends asymptotically to the eigenenergy of the pairing collective mode $z_{\mathbf{q}}^{(T_c)}$ found in section III. This demonstrates that the collective phenomenon we described near T_c proceeds neither from the Anderson-Bogoliubov sound branch, nor from the pair-breaking “Higgs” branch which are characteristic of the low-temperature collective response. The appearance of new poles in the analytic continuation, together with the change in the dispersion relation, suggests that we are dealing with a distinct physical phenomenon: whereas the phononic and pair-breaking branches describe the collective response of the pairs when they form a large fraction of the gas, the pairing mode describes the response of an unpaired, or almost unpaired gas, to externally driven pair formation.

For completeness, we also show on Fig. 13 the poles found in window III (restricted to $q < q_{c3}$) and IV. Both in frequency and damping ω_{III} and ω_{IV} are close to the second pole of window II, $\omega_{\text{IIb}}^{(2)}$ (that is, as long as q is much larger than $1/\xi_{\text{pair}}$). Thus they also tend to $z_{\mathbf{q}}^{(T_c)}$ when $T \rightarrow T_c$. In fact, they represent the same physical resonance: when $T = T_c$, the pair-breaking continuum no longer exhibits the angular points ω_1 , ω_2 and ω_3 (except for $q > 2\sqrt{2m\mu}$ where ω_3 coincides with $\omega_0(q)$); this means that the analytic continuations through windows II to IV become simply equivalent.

At $q > 2\sqrt{2m\mu}$ where only window IV remains, we note that ω_{IV} lies above ω_3 (thus fulfilling the piecewise rule and providing a sensible contribution to the pair field spectral function) in a wide range of values of q . The eigenfrequency then shows a bump when it crosses the pair-breaking continuum edge. At very low $q \ll 1/\xi_{\text{pair}}$, the solution ω_{IV} is subsonic, as one of the solutions found by Ref. [19] at $T = 0$. However it develops the quadratic dispersion described in Sec. III B in the intermediate regime ($1/\xi_{\text{pair}} \ll q \ll k_F$).

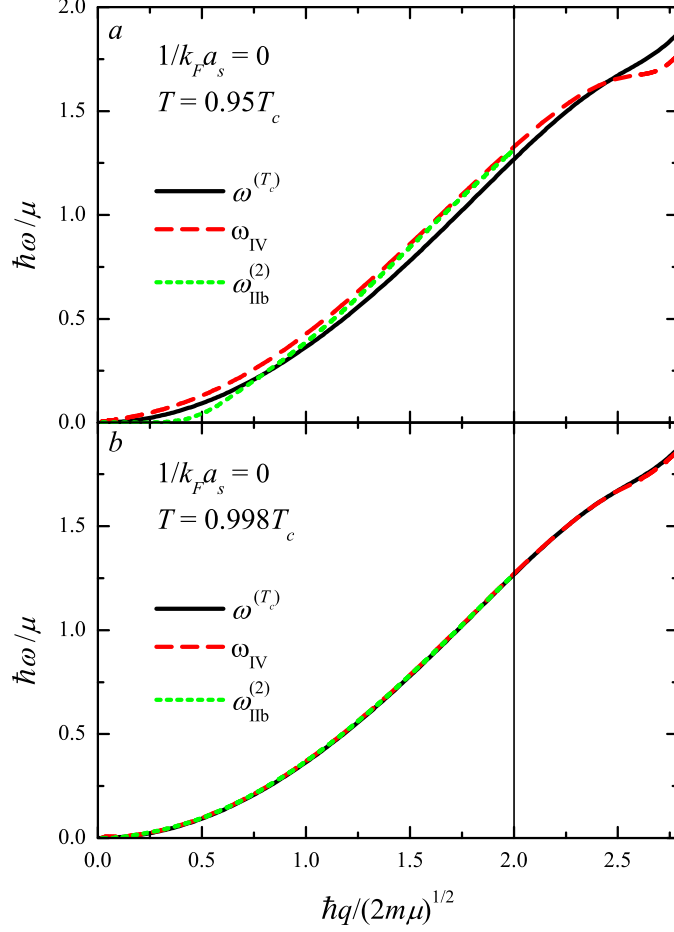


FIG. 14: Momentum dispersion of the frequency of collective modes obtained using the analytic continuation in frequency intervals IIb and IV at $1/(k_F a_s) = 0$ with $T/T_c = 0.95$ (a) and $T/T_c = 0.998$ (b) compared with the eigenfrequency $\omega^{(T_c)}$ determined in Sec. III. The vertical line shows the value of momentum $q = q_{c4} \equiv 2\sqrt{2m\mu}$.

D. Visibility of the collective modes in spectral functions

Now that we have extracted the collective mode spectrum from the analytic continuations (both below (Sec. IV B) and above (Sec. IV C) the pair-breaking continuum), we study the manifestations of this spectrum in the spectral functions. Besides the pair response in the cartesian basis introduced in Eq. (17), we study here the modulus-modulus and phase-phase

spectral functions:

$$\chi_{aa}(\mathbf{q}, \omega) = \frac{1}{\pi} \text{Im} \frac{Q_{1,1}(\mathbf{q}, \omega + i0^+)}{\det \mathbb{Q}(\mathbf{q}, \omega + i0^+)}, \quad (27)$$

$$\chi_{pp}(\mathbf{q}, \omega) = \frac{1}{\pi} \text{Im} \frac{Q_{2,2}(\mathbf{q}, \omega + i0^+)}{\det \mathbb{Q}(\mathbf{q}, \omega + i0^+)}. \quad (28)$$

We note that χ_{aa} , χ_{pp} coincide when $T \rightarrow T_c$ at fixed q . Mathematically, this is because $Q_{11} = Q_{22} = (M_{11} + M_{22})/2$ when M_{12} can be neglected.

1. Residues of the complex poles

a. Phononic branches We first analyse the residues $Z_{\mathbf{q}}$ of different complex poles in χ_{aa} and χ_{pp} . Fig. 15.a shows the residues for the phonon-like branches $z_{1a}^{(1)}$ and $z_{1a}^{(2)}$ as functions of the relative temperature T/T_c for a fixed momentum $q = 0.5\sqrt{2m\mu}$. The value of q is chosen because it lies slightly below the exceptional-point value q_{ex} where the two poles undergo a head-on collision. Panel 15.a then illustrates the behavior of the residues near the exceptional point. The absolute values $|Z_{1a}^{(1)}|$ and $|Z_{1a}^{(2)}|$ of the residues of the two phononic modes show a resonant increase near T_{ex} (we checked numerically their divergence when $(q, T) \rightarrow (q_{ex}, T_{ex})$). However, because residues are complex and the phase of the residues are opposite at resonance, this does not result in a resonant enhancement of the spectral function when the temperature passes T_{ex} , as will be shown below in Fig. 16. The residues of the first and second modes remain close (in absolute value) in the whole considered interval of temperatures (both in the phase-phase and modulus-modulus channels). What determines the domination of $z_{1a}^{(2)}$ over $z_{1a}^{(1)}$ in the spectral functions at temperatures $T_c - T \ll T_c - T_{ex}$ (and vice-versa the domination of $z_{1a}^{(1)}$ over $z_{1a}^{(2)}$ at $T \ll T_{ex}$) is rather the crossing of the damping factors near T_{ex} (see panel 15.b). In the light of this analysis, the critical regime for wavevectors comparable to q_{ex} , appears to be limited to $|T_c - T| \ll |T_c - T_{ex}|$ (which, in the weak-coupling regime, is much more stringent than $|T_c - T| \ll T_c$).

The comparison of the phase and modulus residues also shows a clear domination of the phase channel (recall that in the long wavelength limit [15] one has $|Z_{1a, \text{phase-phase}}| \gg |Z_{1a, \text{modulus-modulus}}|$) except in the vicinity of T_c where they converge to the same value, as expected.

b. Poles of window II Panel c represents the residues of the two modes obtained using the analytic continuation through the window IIb: the pair-breaking “Higgs” mode with

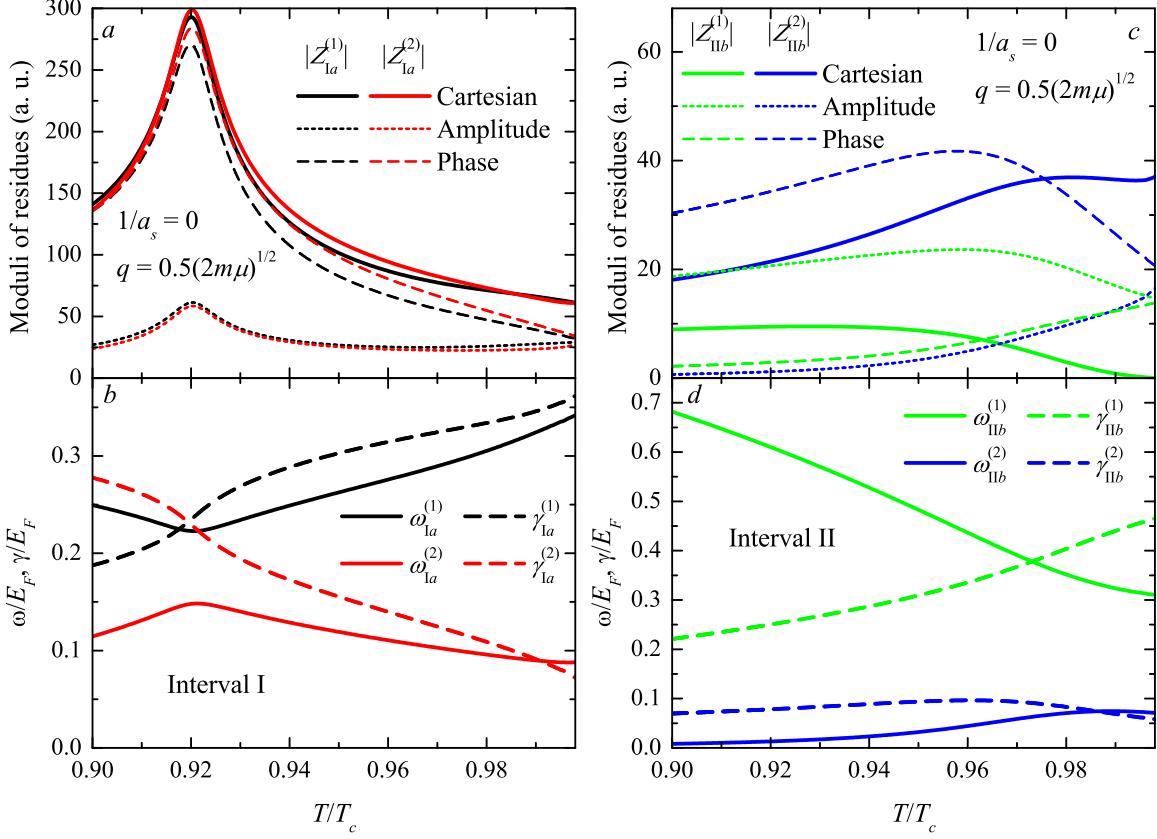


FIG. 15: (a, c) Moduli collective mode residues in the cartesian channel (of spectral function χ , *solid curves*), amplitude-amplitude channel (*dotted curves*) and phase-phase channel (*dashed curves*) as functions of the relative temperature T/T_c for the inverse scattering length $1/a_s = 0$ and the momentum $q = 0.5\sqrt{2m\mu}$. (b, d) Frequencies (*solid curves*) and damping factors (*dashed curves*) for the same collective excitations. Panels (a, b) and (c, d) show collective excitations of window Ia (below the continuum) and IIb (inside the continuum), respectively. The exceptional point here is $(q_{ex}, T_{ex}) \approx (0.556\sqrt{2m\mu}, 0.933T_c)$.

the complex pole $z_{\text{IIb}}^{(1)}$ and the second mode $z_{\text{IIb}}^{(2)}$ of the same window, which tends to the pairing mode $z_{\text{q}}^{(T_c)}$ when $T \rightarrow T_c$. The eigenfrequencies and damping factors for these poles are shown in Fig. 15 d. This further illustrates how the pairing mode of Sec. III replaces the pair-breaking mode as T approaches T_c : in the cartesian spectral function χ , the residue of $z_{\text{IIb}}^{(1)}$ tends to 0 in the cartesian spectral function χ . Even in the modulus-modulus channel the residue of $z_{\text{IIb}}^{(2)}$ eventually dominates over that of $z_{\text{IIb}}^{(1)}$. This effect adds up to a purely spectral effect (see panel d): the pair-breaking mode $z_{\text{IIb}}^{(1)}$ becomes overdamped near T_c while the other mode $z_{\text{IIb}}^{(2)}$ exhibits the opposite trend, it is overdamped at lower temperatures,

and its damping decreases when T approaches T_c .

2. Analytic simulations of the spectral functions

We now wish to measure the amount of information on the spectral functions which is contained in the spectrum and residues found in the analytic continuation. For this, we define (as in Ref. [15]) “analytic simulations” of the spectral functions using the poles $z_{\mathbf{q}}$ and residues $Z_{\mathbf{q}}$ in each of the 5 continuation windows:

$$\chi_{\text{eff}}(\mathbf{q}, \omega) = \sum_{n=1}^5 \sum_{j_n} \delta\chi_n^{(j_n)}(\mathbf{q}, \omega), \quad (29)$$

$$\delta\chi_n^{(j_n)}(\mathbf{q}, \omega) = \frac{1}{\pi} \text{Im} \left(\frac{Z_{\mathbf{q},n}^{(j_n)}}{\omega - z_{\mathbf{q},n}^{(j_n)}} \right) \Theta(\Omega_{n-1} < \omega < \Omega_n), \quad (30)$$

where the index n in a partial contribution $\delta\chi_n^{(j_n)}$ indicates the interval used for the analytic continuation, and j_n labels the complex poles of the GPF propagator continued through this interval. Here, $\{\Omega_n\}$ are the angular-point frequencies as described above, completed by $\Omega_0 \equiv 0$ and $\Omega_5 \rightarrow \infty$ and sorted in the ascending order as follows: $\Omega_1 \equiv \min(\omega_1, \omega_2^{(ph)})$, $\Omega_2 \equiv \max(\omega_1, \omega_2^{(ph)})$, $\Omega_3 \equiv \omega_2^{(pp)}$, and $\Omega_4 \equiv \omega_3$. Particularly for $q > q_{c3}$, the interval between $\omega_2^{(pp)}$ and ω_3 shrinks to zero and does not contribute to χ_{eff} . The Heaviside step function $\Theta(\Omega_{n-1} < \omega < \Omega_n)$ is used on the same reasoning as in Ref. [15]: poles from an analytic continuation are relevant for the spectral function only in the interval through which the analytic continuation passed. It should be noted that the step function means the piecewise rule for the argument ω of the spectral function but *not* a piecewise rule for complex poles $z_{\mathbf{q},n}^{(j_n)}$. For a fixed contribution $\chi_n^{(j_n)}(\mathbf{q}, \omega)$, real parts of relevant poles may move beyond the interval $\Omega_{n-1} < \omega < \Omega_n$, as discussed in the caption of Fig. 6.

In Fig. 16.a, b, c, the spectral function $\chi(\mathbf{q}, \omega)$ and its analytic simulation $\chi_{\text{eff}}(\mathbf{q}, \omega)$ are shown for the same momentum $q = 0.5\sqrt{2m\mu}$ as chosen in Fig. 15, for three temperatures: below, near and above the crossing-point temperature T_{ex} for damping factors. Also, partial contributions of different poles to χ_{eff} are plotted. Fig. 16.d for $T = 0.99T_c$ and a larger wavevector ($q = \sqrt{2m\mu}$) shows the spectral function and its analytic simulation when temperature moves closer to T_c and the momentum is sufficiently large so that the resonance peak lies in the pair-breaking continuum. We note that since the residues are complex, the partial contributions to χ_{eff} are not everywhere positive.

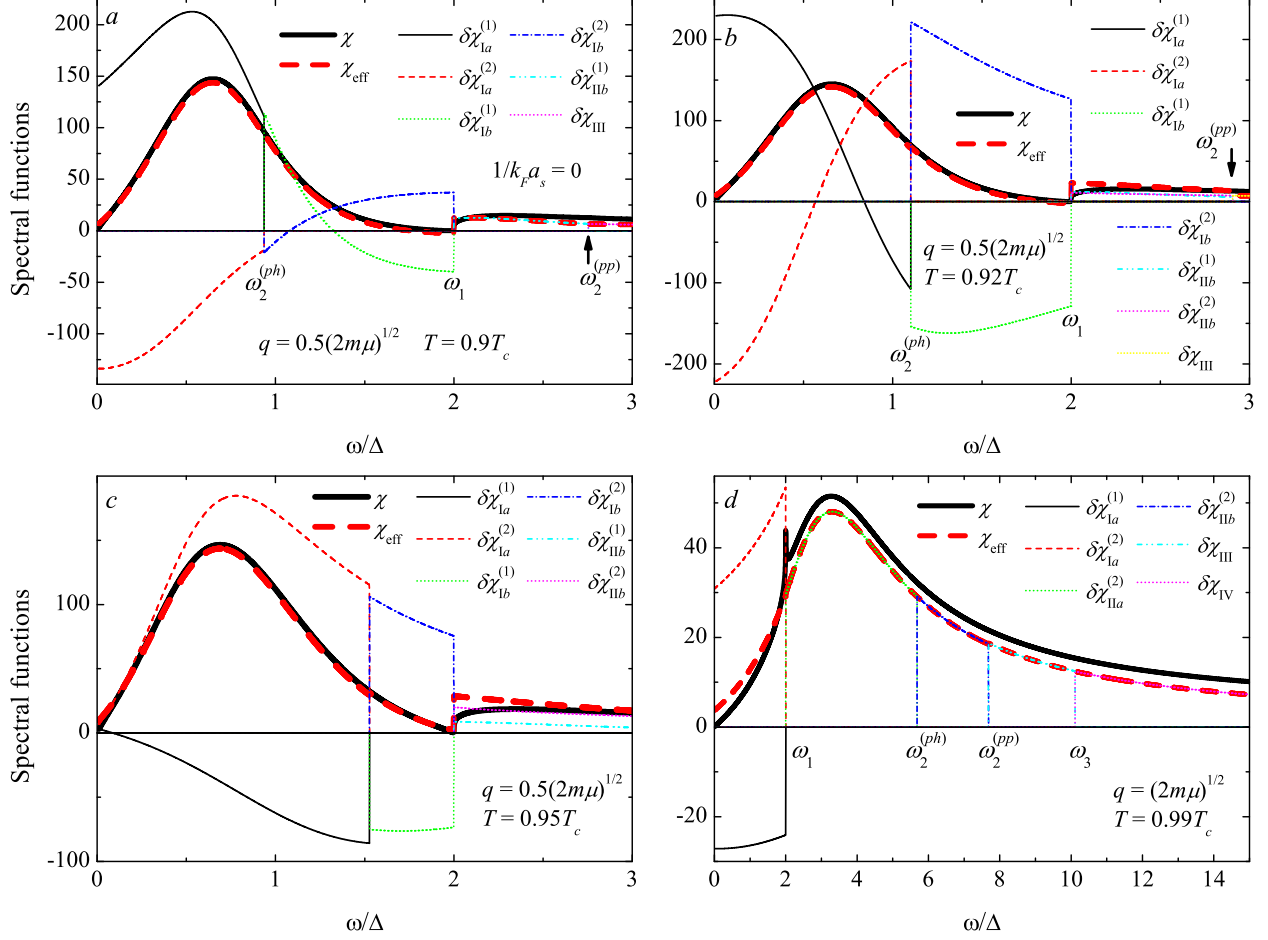


FIG. 16: Spectral function $\chi(\mathbf{q}, \omega)$ (heavy black solid curve), its analytic simulation $\chi_{\text{eff}}(\mathbf{q}, \omega)$ (heavy red dashed curve) and partial contributions of different complex poles (thin curves) as functions of the frequency for the inverse scattering length $1/a_s = 0$ and the momentum $q = 0.5\sqrt{2m\mu}$ (a, b, c) and $q = \sqrt{2m\mu}$ (d) at the temperatures $T = 0.9T_c$ (a), $T = 0.92T_c$ (b), $T = 0.95T_c$ (c), and $T = 0.99T_c$ (d).

In all four panels of (16), we observe that the total analytic simulation is remarkably close to the spectral function χ . This indicates that the poles found in the analytic continuation are a good summary of the shape of the spectral function. When the frequency ω passes a bound between two neighboring intervals for the analytic continuation, the retained partial contributions abruptly change due to the Heaviside function in (29). In some cases, this leads to a well expressed discontinuity of χ_{eff} at a “sharp” angular point, as on panels 16 a,b,c at $\omega = \omega_1$. In other cases, the discontinuity of χ_{eff} is much smaller than the average value of the function, such that the discontinuity at a “soft” angular point is hardly resolvable by

eye. This happens either because two adjacent intervals have almost the same poles in their analytic continuation, and hence almost equal partial contributions (the case of panel 16 *d* at ω_2^{ph} , ω_2^{pp} and ω_3), or, more subtly, because two partial contributions add up to almost the same value of χ_{eff} , despite having an important discontinuity at the angular point (the case of panel 16 *b* at ω_2^{ph}). This distinction between the “sharp” angular point (ω_1) and “soft” ones (ω_2^{ph} , ω_2^{pp} and ω_3) has a physical origin: at the soft angular points only the configuration of resonant wavevectors changes, not the damping mechanism itself. On the contrary, ω_1 separates regions where the damping channel by emission of broken pairs is either opened or closed. This being said, we note that the sharpness of ω_1 decreases when $T \rightarrow T_c$ at fixed q (see panel 16 *d*). This is expected: at $T \geq T_c$ the quasiparticle-quasiparticle continuum is no longer distinguishable from the rest of the particle-hole continuum.

Having a comparable residue, the two phononic poles have overall comparable contributions. At the resonance of residues (Fig. 16 *b*) the two poles participate in the peak of χ_{eff} almost equally. When $T \rightarrow T_c$, the broadening of the partial contribution of $z_{\text{Ia}}^{(1)}$ makes its contribution near the peak of χ_{eff} comparatively smaller. It should be noted that the resonance of residues is not manifested in the temperature behavior of the total spectral function. Moreover, the change of a dominant partial contribution can hardly be distinguished in the total response, and can be extracted only using the analytic simulation.

When T approaches T_c (Fig. 16 *d*), the maximum of the pair field response enters the pair-breaking continuum. In windows IIa and IIb, the main peak almost entirely proceeds from $\delta\chi_{\text{II}}^{(2)}$, the contribution of the first pole (the pair-breaking “Higgs mode”) being negligible. The peak extends almost without discontinuity or angular points onto window III and IV. This does not surprise us since $z_{\text{IIa}}^{(2)}$, z_{IIb} and z_{III} and z_{IV} all tend asymptotically to each other and to the T_c pairing mode $z^{(T_c)}$ analyzed in Sec. III (recall Fig. 14). Near T_c , the angular points separating those 4 intervals tend to disappear, which makes the analytic continuation through the 4 windows nearly equivalent. Although the discussion is purely formal since the intervals are equivalent, we note that the width of windows IIb and III tends to 0 as $T \rightarrow T_c$ such that only intervals IIa and IV remain.

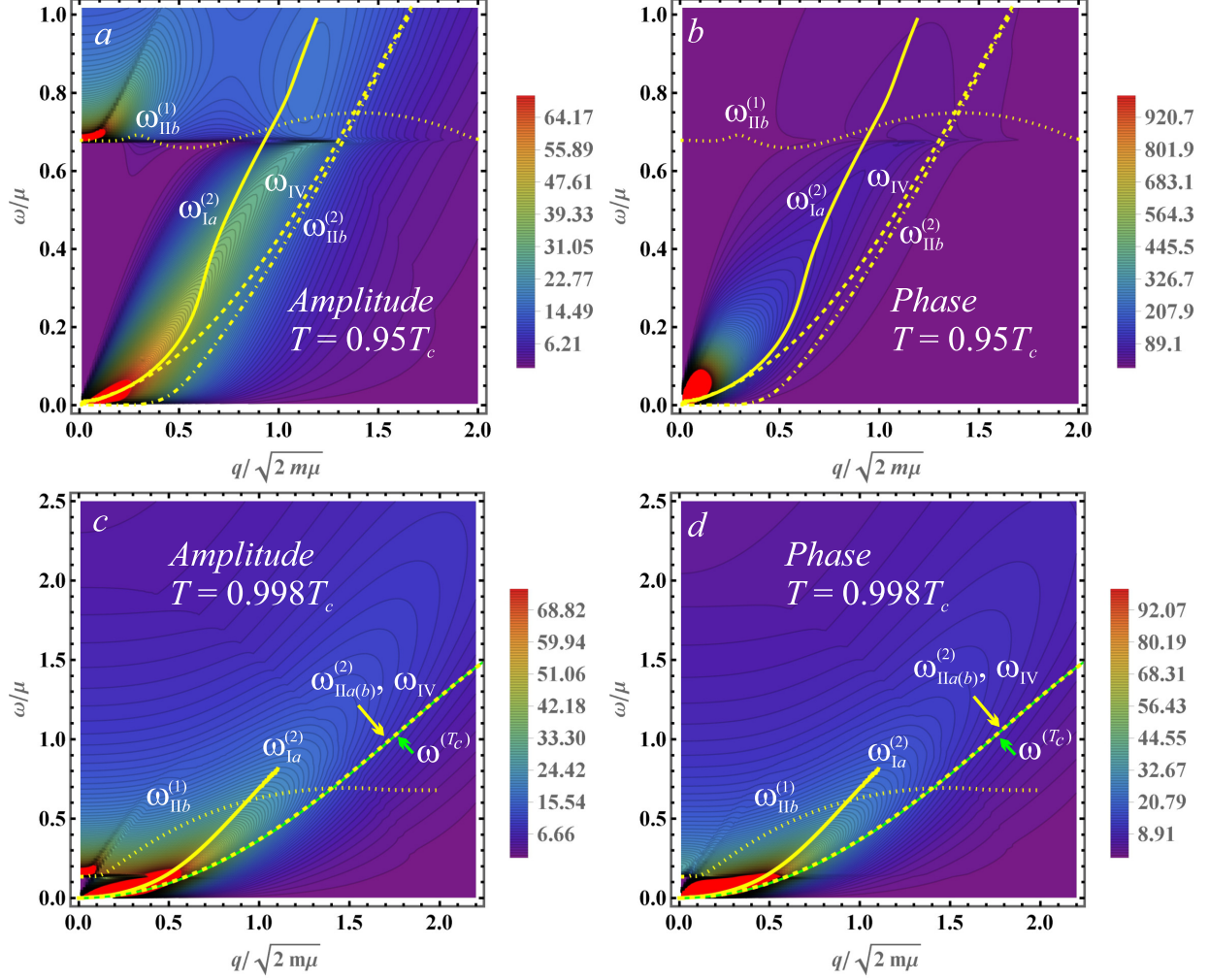


FIG. 17: Contour plots of amplitude-amplitude (a, c) and phase-phase (b, d) response functions for $1/(k_F a_s) = 0$ at $T/T_c = 0.95$ (a, b) and $T/T_c = 0.998$ (c, d). Yellow curves show eigenfrequencies determined by poles of the GPF propagator. The green curves show eigenfrequencies for the GPF propagator at $T = T_c$. Clipping areas above the upper limits in color codes are shown by red.

3. Emergence of the critical regime for collective modes

To better illustrate how the spectral function evolves from a phonon/Higgs mode regime at low temperature, to a critical regime dominated by the quadratic pairing mode, we show on Fig. 17 contour plots of the modulus-modulus and phase-phase spectral functions. On top of the contour plots, we indicate selected eigenfrequencies from roots of Eq.(3). Here, only the roots which give the most significant contributions to the spectral functions have

been plotted⁶. As T approaches T_c , the region of energy-momentum where the influence of the phononic-like modes $\omega_{\text{Ia}}^{(1,2)}$ and pair-breaking mode $\omega_{\text{IIb}}^{(1)}$ shrinks to a small window $q \lesssim 1/\xi_{\text{pair}}$ and $\omega \lesssim \Delta$, corresponding to the region where the existence of condensed pairs still matters. Elsewhere, the spectral function is dominated by a resonance well summarized by $z^{(T_c)} \approx z_{\text{IIa}}^{(2)} \approx z_{\text{IIb}}^{(2)} \approx z_{\text{IV}}$ (and the associated residue⁷). Fig. 17 thus illustrates the reduction of the phononic/pair-breaking regime when $T \rightarrow T_c$, and the corresponding growth of a critical regime dominated by the pairing collective mode $z_{\mathbf{q}}^{(T_c)}$. Again we note that χ_{aa} and χ_{pp} coincide when $T \rightarrow T_c$ at fixed q as is clearly visible on the lower panels of Fig. 17.

V. CONCLUSIONS

We have investigated collective excitations in condensed Fermi gases in the whole range of the BCS-BEC crossover for finite temperatures below T_c and beyond the small-momentum approximation. Eigenfrequencies and damping factors for different branches of collective excitations are calculated within the Gaussian pair fluctuation approach using a unified method of finding complex poles of the analytically continued GPF propagator. The real and imaginary parts of complex poles are calculated mutually consistently, beyond the perturbation theory for damping. This makes it possible to consider collective excitations also in cases when damping is not small.

At and near T_c , we showed that a quadratically-dispersed collective mode, acting as a precursor of the phase transition, is observable in the response of the system to a driving pairing field. This mode was predicted by Andrianov and Popov in the BCS limit [22] and appears in the dissipative time-dependent Ginzburg-Landau equation of Ref. [20]. We

⁶ Here, the choice between “ a ” and “ b ” windows needs an explanation. It depends on the fact whether the analytic simulation χ_{eff} using this window is appropriate to reproduce the spectral function χ . More clearly, for $T = 0.95T_c$, the “Higgs” mode lies above the angular-point frequency $\omega_2^{(ph)}$ in the range of momenta where it is not overdamped. The sound-like mode frequencies at the same temperature are mainly lower than $\omega_2^{(ph)}$. Consequently, we plot here $\omega_{\text{Ia}}^{(2)}$, $\omega_{\text{IIb}}^{(1)}$, and $\omega_{\text{IIb}}^{(2)}$, choosing the interval “ a ” for sound-like modes and “ b ” for modes in the continuum. Also, this explains a choice of representative intervals for the analytic continuation in Fig. 15. On the contrary, at $T = 0.998T_c$, the angular-point frequency $\omega_2^{(ph)}$ appears to be higher than $\omega_{\text{IIa(b)}}^{(2)}$ in the range of q where the mode is not overdamped. Therefore the window “ a ” is relevant for Fig. 17 (c, d).

⁷ We note that $T = 0.998T_c$ and $q > 0.5\sqrt{2m\mu}$, the complex residue clearly shifts the peak of the resonance away from $\omega^{(T_c)}$.

computed analytically its effective mass and showed how it varies from purely imaginary values in the BCS limit to purely real in the BEC limit. Away from T_c we computed (to leading order in $|T - T_c|$) the energy shift, which acts as a gap in the BEC regime and as an extra damping rate in the BCS limit. Last, we explained how the resonance disappears at large q when it encounters the lower-edge of the pairing continuum.

We note that the drastic change in the dispersion of the collective modes is predicted here within GPF theory, which approximates the correlation length critical exponent to its BCS value $\nu = 1/2$, in disagreement of about 25% with the calculated value for the universality class of superfluid Fermi gases [25, 26]. Integrating this correction to the study of collective modes in the critical regime would certainly make the prediction more quantitative. Our approach also assumes an infinite quasiparticle lifetime, which restricts us for the study of collective modes to the collisionless regime. Extending our analysis to the hydrodynamic regime, where excitations analogous to Carlson-Goldman modes are expected, will be an important step forward. This requires a precise estimate of the quasiparticle lifetime, which, in an ultracold Fermi gas weakly coupled to its environment, should be limited by intrinsic processes such as quasiparticle collisions.

Away from the limits $T \rightarrow T_c$ and $q \rightarrow 0$, our general study allows us to track the evolution of different branches of collective excitations, and to make clear genetic relations between them. Particularly, we show that the collective mode near the transition temperature is genetically distinct from both pair-breaking and phononic modes (whose visibility domain shrinks to a small window $\omega \lesssim \Delta$ and $q \lesssim 1/\xi_{\text{pair}}$ near T_c) as it is caused by the appearance of new poles in the analytic continuation. At $0 < T < T_c$, eigenfrequencies and damping factors exhibit a nontrivial momentum and temperature dependence. Particularly, they can be non-monotonic as functions of q . Moreover, different eigenfrequencies may cross each other and change their relative significance when varying momentum and temperature. The present study clarifies then some unexplored questions in the theory of collective excitations in superfluid Fermi gases. The applied method can be straightforwardly extended to more complicated condensed fermionic systems, e. g., multiband or color superfluids.

Appendix A: Fluctuation matrix

We recall here the elements of the order-parameter fluctuation matrix \mathbb{Q} in modulus-phase basis (for the matrix \mathbb{M} , in the cartesian basis see Eqs. (10) and (11) in [15]).

$$\begin{aligned}
Q_{1,1}(\mathbf{q}, z) = & -\frac{1}{8\pi a_s} + \int \frac{d\mathbf{k}}{(2\pi)^3} \left\{ \frac{1}{2k^2} + \frac{X\left(\beta E_{\mathbf{k}-\frac{\mathbf{q}}{2}}\right)}{4E_{\mathbf{k}-\frac{\mathbf{q}}{2}}E_{\mathbf{k}+\frac{\mathbf{q}}{2}}} \right. \\
& \times \left[\left(\xi_{\mathbf{k}-\frac{\mathbf{q}}{2}}\xi_{\mathbf{k}+\frac{\mathbf{q}}{2}} + E_{\mathbf{k}-\frac{\mathbf{q}}{2}}E_{\mathbf{k}+\frac{\mathbf{q}}{2}} - \Delta^2 \right) \left(\frac{1}{z - E_{\mathbf{k}-\frac{\mathbf{q}}{2}} - E_{\mathbf{k}+\frac{\mathbf{q}}{2}}} - \frac{1}{z + E_{\mathbf{k}-\frac{\mathbf{q}}{2}} + E_{\mathbf{k}+\frac{\mathbf{q}}{2}}} \right) \right. \\
& \left. \left. + \left(\xi_{\mathbf{k}-\frac{\mathbf{q}}{2}}\xi_{\mathbf{k}+\frac{\mathbf{q}}{2}} - E_{\mathbf{k}-\frac{\mathbf{q}}{2}}E_{\mathbf{k}+\frac{\mathbf{q}}{2}} - \Delta^2 \right) \left(\frac{1}{z - E_{\mathbf{k}+\frac{\mathbf{q}}{2}} + E_{\mathbf{k}-\frac{\mathbf{q}}{2}}} - \frac{1}{z - E_{\mathbf{k}-\frac{\mathbf{q}}{2}} + E_{\mathbf{k}+\frac{\mathbf{q}}{2}}} \right) \right] \right\}, \quad (\text{A1})
\end{aligned}$$

$$\begin{aligned}
Q_{2,2}(\mathbf{q}, z) = & -\frac{1}{8\pi a_s} + \int \frac{d\mathbf{k}}{(2\pi)^3} \left\{ \frac{1}{2k^2} + \frac{X\left(\beta E_{\mathbf{k}-\frac{\mathbf{q}}{2}}\right)}{4E_{\mathbf{k}-\frac{\mathbf{q}}{2}}E_{\mathbf{k}+\frac{\mathbf{q}}{2}}} \right. \\
& \times \left[\left(\xi_{\mathbf{k}-\frac{\mathbf{q}}{2}}\xi_{\mathbf{k}+\frac{\mathbf{q}}{2}} + E_{\mathbf{k}-\frac{\mathbf{q}}{2}}E_{\mathbf{k}+\frac{\mathbf{q}}{2}} + \Delta^2 \right) \left(\frac{1}{z - E_{\mathbf{k}-\frac{\mathbf{q}}{2}} - E_{\mathbf{k}+\frac{\mathbf{q}}{2}}} - \frac{1}{z + E_{\mathbf{k}-\frac{\mathbf{q}}{2}} + E_{\mathbf{k}+\frac{\mathbf{q}}{2}}} \right) \right. \\
& \left. \left. + \left(\xi_{\mathbf{k}-\frac{\mathbf{q}}{2}}\xi_{\mathbf{k}+\frac{\mathbf{q}}{2}} - E_{\mathbf{k}-\frac{\mathbf{q}}{2}}E_{\mathbf{k}+\frac{\mathbf{q}}{2}} + \Delta^2 \right) \left(\frac{1}{z - E_{\mathbf{k}+\frac{\mathbf{q}}{2}} + E_{\mathbf{k}-\frac{\mathbf{q}}{2}}} - \frac{1}{z - E_{\mathbf{k}-\frac{\mathbf{q}}{2}} + E_{\mathbf{k}+\frac{\mathbf{q}}{2}}} \right) \right] \right\}, \quad (\text{A2})
\end{aligned}$$

$$\begin{aligned}
Q_{1,2}(\mathbf{q}, z) = & i \int \frac{d\mathbf{k}}{(2\pi)^3} \frac{X\left(\beta E_{\mathbf{k}-\frac{\mathbf{q}}{2}}\right)}{4E_{\mathbf{k}-\frac{\mathbf{q}}{2}}E_{\mathbf{k}+\frac{\mathbf{q}}{2}}} \\
& \times \left[\left(\xi_{\mathbf{k}-\frac{\mathbf{q}}{2}}E_{\mathbf{k}+\frac{\mathbf{q}}{2}} + E_{\mathbf{k}-\frac{\mathbf{q}}{2}}\xi_{\mathbf{k}+\frac{\mathbf{q}}{2}} \right) \left(\frac{1}{z - E_{\mathbf{k}-\frac{\mathbf{q}}{2}} - E_{\mathbf{k}+\frac{\mathbf{q}}{2}}} + \frac{1}{z + E_{\mathbf{k}-\frac{\mathbf{q}}{2}} + E_{\mathbf{k}+\frac{\mathbf{q}}{2}}} \right) \right. \\
& \left. + \left(\xi_{\mathbf{k}-\frac{\mathbf{q}}{2}}E_{\mathbf{k}+\frac{\mathbf{q}}{2}} - E_{\mathbf{k}-\frac{\mathbf{q}}{2}}\xi_{\mathbf{k}+\frac{\mathbf{q}}{2}} \right) \left(\frac{1}{z - E_{\mathbf{k}+\frac{\mathbf{q}}{2}} + E_{\mathbf{k}-\frac{\mathbf{q}}{2}}} + \frac{1}{z - E_{\mathbf{k}-\frac{\mathbf{q}}{2}} + E_{\mathbf{k}+\frac{\mathbf{q}}{2}}} \right) \right], \quad (\text{A3})
\end{aligned}$$

$$Q_{2,1}(\mathbf{q}, z) = -Q_{1,2}(\mathbf{q}, z). \quad (\text{A4})$$

where we use $\hbar = k_B = 2m = 1$ and $E_{\mathbf{k}} = \sqrt{\xi_{\mathbf{k}}^2 + \Delta^2}$ is the BCS excitation energy, $\xi_{\mathbf{k}} = k^2 - \mu$ is the free-fermion energy, and X is the function

$$X(t) = \tanh\left(\frac{t}{2}\right), \quad (\text{A5})$$

These matrix elements coincide with those introduced in Refs. [16].

Appendix B: Details on the long wavelength calculation near T_c

We give here more details on the calculation of the collective mode spectrum leading to expression (11) above T_c and (13) below T_c . Above T_c , we add and subtract the sum $\sum_{\mathbf{k}} X(\beta\xi_{\mathbf{k}})/2\xi_{\mathbf{k}}$ to M_{11} , leading to:

$$M_{11}(z, \mathbf{q}, \beta < \beta_c) = I_1(z, \mathbf{q}, \beta) + I_0(\beta) \quad (\text{B1})$$

with

$$I_1(z, \mathbf{q}, \beta) = \sum_{\mathbf{k}} \frac{X(\beta\xi_+) + X(\beta\xi_-)}{2(z - \xi_+ - \xi_-)} + \sum_{\mathbf{k}} \frac{X(\beta\xi_{\mathbf{k}})}{2\xi_{\mathbf{k}}} \quad (\text{B2})$$

$$I_0(\beta) = \sum_{\mathbf{k}} \frac{X(\beta_c\xi_{\mathbf{k}}) - X(\beta\xi_{\mathbf{k}})}{2\xi_{\mathbf{k}}} = -\frac{\beta - \beta_c}{2} \sum_{\mathbf{k}} X'(\beta_c\xi_{\mathbf{k}}) + O(\beta - \beta_c)^2 \quad (\text{B3})$$

Omitting terms of order $(\beta - \beta_c)q^2/2m$, one can then approximate I_1 by its value in $\beta = \beta_c$:

$$I_1(\omega \pm i0^+, \mathbf{q}, \beta_c) = C \frac{q^2}{2m} - D'\omega \mp iD''\omega \quad (\text{B4})$$

Below T_c , one should take into account the non-vanishing off-diagonal matrix element M_{12} as well as the deviation of the diagonal elements $M_{11}(\Delta) - M_{11}(0)$ due to the non-zero value of the gap. We compute the latter quantity by setting $z = 0$ before expanding for $q \rightarrow 0$:

$$\begin{aligned} M_{11}(z = 0, \mathbf{q}, \Delta(T), T) - M_{11}(z = 0, \mathbf{q}, \Delta = 0, T) &= \\ \sum_{\mathbf{k}} \left[\frac{X(\beta\xi_{\mathbf{k}})}{2\xi_{\mathbf{k}}} - \frac{X(\beta\epsilon_{\mathbf{k}})}{2\epsilon_{\mathbf{k}}} \right] - \Delta^2 \sum_{\mathbf{k}} \frac{\beta\epsilon_{\mathbf{k}}X'(\beta\epsilon_{\mathbf{k}}) - X(\beta\epsilon_{\mathbf{k}})}{4\epsilon_{\mathbf{k}}^3} + O(q^2) & \\ = -2I_0(\beta) + O(\beta - \beta_c)^2 & \quad (\text{B5}) \end{aligned}$$

To recognize $-I_0$ in the first sum of the right-hand-side of (B5), we have used the gap equation in the form

$$\sum_{\mathbf{k}} \frac{X(\beta\epsilon_{\mathbf{k}})}{2\epsilon_{\mathbf{k}}} = \sum_{\mathbf{k}} \frac{X(\beta_c\xi_{\mathbf{k}})}{2\xi_{\mathbf{k}}} \quad (\text{B6})$$

For the second sum, we use the link between Δ^2 and $\beta - \beta_c$ obtained by expanding (B6) for $\beta \rightarrow \beta_c$ with $\Delta^2 \propto \beta - \beta_c$:

$$\Delta^2 \sum_{\mathbf{k}} \frac{\beta_c\xi_{\mathbf{k}}X'(\beta_c\xi_{\mathbf{k}}) - X(\beta_c\xi_{\mathbf{k}})}{4\xi_{\mathbf{k}}^3} = I_0(\beta) + O(\beta - \beta_c)^2 = (\beta - \beta_c)E + O(\beta - \beta_c)^2 \quad (\text{B7})$$

We then approximate

$$M_{11,\downarrow}(z, \mathbf{q}, \Delta, T) \simeq M_{11,\downarrow}(z, \mathbf{q}, 0, T) + M_{11}(0, \mathbf{q}, \Delta, T) - M_{11}(0, \mathbf{q}, 0, T) \\ \simeq C \frac{q^2}{2m} - (D' + iD'')z - (\beta - \beta_c)E(\beta_c\mu) \quad (\text{B8})$$

To compute $M_{22,\downarrow}$, we use the equality on the real axis $M_{22}(\omega + i0^+) = M_{11}(-\omega - i0^+)$ before doing the analytic continuation

$$M_{22,\downarrow}(z, \mathbf{q}, \Delta, T) \simeq C \frac{q^2}{2m} + (D' - iD'')z - (\beta - \beta_c)E(\beta_c\mu) \quad (\text{B9})$$

Finally, for the off-diagonal element M_{12} , the value in $z = 0$, $q \rightarrow 0$ suffices to leading order in $\beta - \beta_c$:

$$M_{12}(0, \mathbf{q}, \Delta, \beta) = -\Delta^2 \sum_{\mathbf{k}} \frac{X(\beta\epsilon) - \beta\epsilon X'(\beta\epsilon)}{4\epsilon^3} + O(q^2) = I_0(\beta) + O(\beta - \beta_c)^2 \quad (\text{B10})$$

Acknowledgments

We acknowledge financial support from the Research Foundation-Flanders (FWO-Vlaanderen) Grant No. G.0618.20.N, and from the research council of the University of Antwerp.

-
- [1] G. C. Strinati, P. Pieri, G. Röpke, P. Schuck, and M. Urban, *The BCS–BEC crossover: From ultra-cold Fermi gases to nuclear systems*, Physics Reports **738**, 1 (2018).
 - [2] M. Yu. Kagan and A.V. Turlapov, *BCS-BEC crossover, collective excitations and superfluid hydrodynamics in quantum fluids and gases*, Physics-Uspekhi, **188**, 225 (2019).
 - [3] M. Bartenstein, A. Altmeyer, S. Riedl, S. Jochim, C. Chin, J. H. Denschlag, and R. Grimm, *Collective Excitations of a Degenerate Gas at the BEC-BCS Crossover*, Phys. Rev. Lett. **92**, 203201 (2004).
 - [4] J. Kinast, A. Turlapov, and J. E. Thomas, *Damping of a Unitary Fermi Gas*, Phys. Rev. Lett. **94**, 170404 (2005).
 - [5] A. Altmeyer, S. Riedl, C. Kohstall, M. J. Wright, R. Geursen, M. Bartenstein, C. Chin, J. Hecker Denschlag, and R. Grimm, *Precision Measurements of Collective Oscillations in the BEC-BCS Crossover*, Phys. Rev. Lett. **98**, 040401 (2007).

- [6] M. K. Tey, L. A. Sidorenkov, E. R. S. Guajardo, R. Grimm, M. J. H. Ku, M. W. Zwierlein, Y.-H. Hou, L. Pitaevskii, and S. Stringari, *Collective Modes in a Unitary Fermi Gas across the Superfluid Phase Transition*, Phys. Rev. Lett. **110**, 055303 (2013).
- [7] L. A. Sidorenkov, M. K. Tey, R. Grimm, Y.-H. Hou, L. Pitaevskii, and S. Stringari, *Second sound and the superfluid fraction in a Fermi gas with resonant interactions*, Nature (London) **498**, 78 (2013).
- [8] S. Hoinka, P. Dyke, M. G. Lingham, J. J. Kinnunen, G. M. Bruun, and C. J. Vale, *Goldstone mode and pair-breaking excitations in atomic Fermi superfluids*, Nat. Phys. **13**, 943 (2017).
- [9] C. C. N. Kuhn, S. Hoinka, I. Herrera, P. Dyke, J. J. Kinnunen, G. M. Bruun, and C. J. Vale, *High-Frequency Sound in a Unitary Fermi Gas*, Phys. Rev. Lett. **124**, 150401 (2020).
- [10] R. Combescot, M. Yu. Kagan, and S. Stringari, *Collective mode of homogeneous superfluid Fermi gases in the BEC-BCS crossover*, Phys. Rev. A **74**, 042717 (2006).
- [11] R. B. Diener, R. Sensarma, and M. Randeria, *Quantum fluctuations in the superfluid state of the BCS-BEC crossover*, Phys. Rev. A **77**, 023626 (2008).
- [12] Y. Ohashi and A. Griffin, *Superfluidity and collective modes in a uniform gas of Fermi atoms with a Feshbach resonance*, Phys. Rev. A **67**, 063612 (2003).
- [13] H. Kurkjian, Y. Castin, and A. Sinatra, *Concavity of the collective excitation branch of a Fermi gas in the BEC-BCS crossover*, Phys. Rev. A **93**, 013623 (2016).
- [14] H. Kurkjian and J. Tempere, *Absorption and emission of a collective excitation by a fermionic quasiparticle in a Fermi superfluid*, New J. Phys. **19**, 113045 (2017).
- [15] S. N. Klimin, J. Tempere, and H. Kurkjian, *Phononic collective excitations in superfluid Fermi gases at nonzero temperatures*, Phys. Rev. A **100**, 063634 (2019).
- [16] J. R. Engelbrecht, M. Randeria, and C. A. R. Sá de Melo, *BCS to Bose crossover: Broken-symmetry state*, Phys. Rev. B **55**, 15153 (1997).
- [17] H. Kurkjian, S. N. Klimin, J. Tempere, and Y. Castin, *Pair-Breaking Collective Branch in BCS Superconductors and Superfluid Fermi Gases*, Phys. Rev. Lett. **122**, 093403 (2019).
- [18] H. Kurkjian, J. Tempere, and S. N. Klimin, *Linear response of a superfluid Fermi gas inside its pair-breaking continuum*, Sci. Rep. **10**, 11591 (2020). <https://doi.org/10.1038/s41598-020-65371-9>.
- [19] Y. Castin and H. Kurkjian, *Branche d'excitation collective du continuum dans les gaz de fermions condensés par paires: étude analytique et lois d'échelle*, Comptes Rendus. Physique

- 21**, 253 (2020).
- [20] C. A. R. Sá de Melo, M. Randeria, and J.R. Engelbrecht, *Crossover from BCS to Bose superconductivity: Transition temperature and time-dependent Ginzburg-Landau theory*, Phys. Rev. Lett. **71**, 3202 (1993).
 - [21] Philippe Nozières, *Le problème à N corps: propriétés générales des gaz de fermions* (Dunod, Paris, 1963).
 - [22] V. A. Andrianov and V. N. Popov. *Gidrodinamicheskoe dejstvie i Boze-spektr sverhtekucih Fermi-sistem*. Teor. Mat. Fiz. **28**, 341 (1976). [English translation: Theor. Math. Phys. **28**, 829 (1976)].
 - [23] P. Nozières and S. Schmitt-Rink, *Bose condensation in an attractive fermion gas: From weak to strong coupling superconductivity*, J. Low Temp. Phys. **59**, 195 (1985).
 - [24] R. V. Carlson and A. M. Goldman, *Dynamics of the order parameter of superconducting aluminum films*, J. Low Temp. Phys. **25**, 67 (1976).
 - [25] S. Diehl, S. Floerchinger, H. Gies, J. M. Pawłowski, and C. Wetterich, *Functional renormalization group approach to the BCS-BEC crossover*, Annalen der Physik **522**, 615 (2010).
 - [26] T. Debelhoir and N. Dupuis, *Critical region of the superfluid transition in the BCS-BEC crossover*, Phys. Rev. A **93**, 023642 (2016).
 - [27] E. Taylor, *Critical behavior in trapped strongly interacting Fermi gases*, Phys. Rev. A **80**, 023612 (2009).